Origin of the ankle in the ultrahigh energy cosmic ray spectrum, and of the extragalactic protons below it

Michael Unger,[1,2,*] Glennys R. Farrar,[1,†] and Luis A. Anchordoqui[3,4,5,‡]

[1]*Department of Physics, Center for Cosmology and Particle Physics, New York University, New York, New York 10003, USA*

[2]*Karlsruher Institut für Technologie, Institut für Kernphysik, Postfach 3640, 76021 Karlsruhe, Germany*

[3]*Department of Physics and Astronomy, Lehman College, City University of New York, New York, New York 10468, USA*

[4]*Department of Physics, Graduate Center, City University of New York, 365 Fifth Avenue, New York, New York 10016, USA*

[5]*Department of Astrophysics, American Museum of Natural History, Central Park West 79 Street, New York, New York 10024, USA*

(Received 8 May 2015; revised manuscript received 15 September 2015; published 1 December 2015)

The sharp change in slope of the ultrahigh energy cosmic ray (UHECR) spectrum around $10^{18.6}$ eV (the ankle), combined with evidence of a light but extragalactic component near and below the ankle and intermediate composition above, has proved exceedingly challenging to understand theoretically, without fine-tuning. We propose a mechanism whereby photo-disintegration of ultrahigh energy nuclei in the region surrounding a UHECR accelerator accounts for the observed spectrum and inferred composition at Earth. For suitable source conditions, the model reproduces the spectrum and the composition over the entire extragalactic cosmic ray energy range, i.e. above $10^{17.5}$ eV. Predictions for the spectrum and flavors of neutrinos resulting from this process are also presented.

DOI: 10.1103/PhysRevD.92.123001 PACS numbers: 98.70.Sa, 95.85.Ry, 96.50.sb

I. INTRODUCTION

The cosmic ray spectrum spans roughly eleven decades of energy, 10^9 eV $\lesssim E \lesssim 10^{20}$ eV and has three major features: the steepening of the spectrum dubbed the "knee" at $\approx 10^{15.6}$eV [1], a pronounced hardening of the spectrum at $E \approx 10^{18.6}$ eV, the so-called "ankle" feature [2–4], and finally a cutoff around $10^{19.6}$ eV [3,5]. Three additional more subtle features have been reported between the knee and the ankle: A hardening of the spectrum at around 2×10^{16} eV [6–9] followed by two softenings at $\sim 10^{16.9}$ eV [6,7] and $10^{17.5}$ eV [2,8–11]. The latter is traditionally referred to as the "second knee".

The variations of the spectral index reflect various aspects of cosmic ray production, source distribution and propagation. The first and second knee have straightforward explanations, as reflecting the maximum energy of Galactic magnetic confinement or acceleration capability of the sources, both of which grow linearly in the charge Z of the nucleus; the first knee being where protons drop out and the second knee where the highest-Z Galactic cosmic rays drop out. As the energy increases above the second knee to the ankle, the composition evolves from heavy to light [12] while the cosmic ray arrival directions are isotropic to high accuracy throughout the range [13–15]. Finally, as the energy increases above the ankle, not only does the spectrum harden significantly, but the composition gradually becomes heavier (interpreting the data using conventional extrapolations of accelerator-constrained particle physics models) [16,17].

This observed evolution in the extragalactic cosmic ray composition and spectral index presents a major conundrum. A pure proton composition might be compatible with the observed spectrum of extragalactic cosmic rays [18] when allowance is made for experimental uncertainties in the energy scale and the fact that the real local source distribution is not homogeneous and continuous [19] (although the sharpness of the ankle is difficult to accommodate), but a pure proton composition is incompatible with the depth-of-shower-maximum ($X_{\rm max}$) distributions observed by Auger [16,17] unless current extrapolations of particle physics are incorrect. Moreover, a fit of the spectrum with a pure proton composition seems to require a very strong source evolution [20] which leads to a predicted neutrino flux in excess of experimental limits [21]. On the other hand, models which fit the spectrum and composition at highest energies, predict a deep gap between the end of the Galactic cosmic rays and the onset of the extragalactic cosmic rays [22–27]. Models can be devised to fill this gap, but fine-tuning is required to position this new population so as to just fit and fill the gap [28–30].

Here we offer a resolution to this conundrum, by showing that "post-processing" of UHECRs via

*mu495@nyu.edu
†gf25@nyu.edu
‡laa410@nyu.edu

photo-disintegration in the environment surrounding the source, can naturally explain the entire spectrum and composition. In our model, extragalactic cosmic rays below the ankle are predominantly protons from nucleons knocked off higher energy nuclei in the region surrounding the accelerator, and the spectrum and composition above the ankle are predominantly dictated by the accelerator and propagation to Earth. The model makes distinctive predictions about the spectrum and flavor ratios of neutrinos, which should enable it to be tested. If the ankle and the protons below it arise on account of our mechanism, we obtain a new constraint on UHECR sources beyond the Hillas criterion and total-energy-injection requirements, namely that the environment around the source has the conditions giving rise to the required amount of photo-disintegration.

Up until now, photo-disintegration (PD) has been mainly considered as a danger inside the accelerator, as it would cut off the cosmic ray spectrum at energies such that the PD interaction length and the acceleration length are comparable. Since the acceleration length increases with energy, whereas the PD interaction length generally decreases with energy, photo-dissociation acts as a *low-pass filter*. The insight underlying the mechanism we propose, is that if the primary locus of PD is *outside* the accelerator, PD generally acts as a *high-pass filter*, permitting the highest energy cosmic rays to escape unscathed while the lower energy ones are disintegrated inside the source region, generating nucleons with energy $1/A$ of the original nucleus of mass A. As we shall see, these spallated nucleons naturally produce the ankle feature, explain why extragalactic cosmic rays below the ankle are protonic, and account for the spectral index below the ankle. Examples of systems in which the accelerator is embedded in a photon field and the cosmic rays are trapped by magnetic fields in that environment could be the dusty torus surrounding an active galactic nucleus or the interstellar medium of the star-forming region surrounding most young pulsars; see also [31–38]. The basic setup of our phenomenological model is illustrated in Fig. 1.

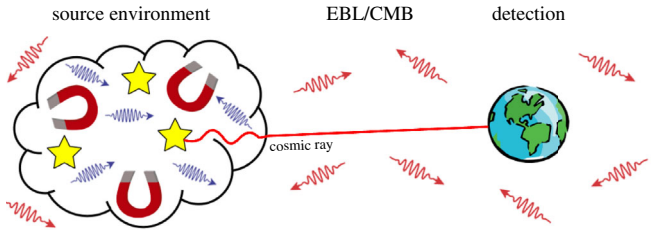

FIG. 1 (color online). Illustration of our model calculation: Sources (yellow stars) inject cosmic rays with a power law in energy, into a surrounding region of radiation and turbulent magnetic fields. After propagation through this local environment and then intergalactic space, these cosmic rays and their spallation products are detected at Earth. The photon energies in the source environment are characteristically of much higher energy than in the extragalactic background light.

The layout of the paper is as follows. In Sec. II we introduce our model and in Sec. III we compare its predictions with experimental data. Details about particle propagation and the calculation of multimessenger signatures are given in the appendices. Section IV contains our conclusions.

II. FORMATION OF THE ANKLE

To illustrate the mechanism we have identified to create the ankle and generate protons below, consider a system in which the accelerator (also referred to as the source) is embedded in an environment in which the cosmic rays are confined for some time by magnetic fields while interacting with the ambient radiation field. Our essential simplifications are: (i) a fast acceleration mechanism and/or a low photon density inside the accelerator, (ii) no energy is lost except through an interaction, and whenever a nucleus interacts it loses one or more nucleons by photo-disintegration or photo-pion production (in this case the nucleus loses a fraction of its energy corresponding to the reduction in its nuclear mass); (iii) a cosmic ray either escapes without changing energy, with a rate $\tau_{\rm esc}$, or the cosmic ray interacts one or more times before escaping; (iv) $\tau_{\rm esc}$ and $\tau_{\rm int}$ are independent of position in the source environment and depend only on $\{E, A, Z\}$ of the nucleus. In this approximation the number of nuclei in a given energy range and with a specified $\{A, Z\}$ decreases exponentially with time, with

$$\tau = (\tau_{\rm esc}^{-1} + \tau_{\rm int}^{-1})^{-1}. \tag{1}$$

A fraction

$$\eta_{\rm esc} = (1 + \tau_{\rm esc}/\tau_{\rm int})^{-1} \tag{2}$$

of the particles escape without interaction and the rest interact before escaping, so $\eta_{\rm int} = 1 - \eta_{\rm esc}$. Note that $\eta_{\rm esc}$ and $\eta_{\rm int}$ depend only on the ratio of the escape and interaction times, but not on the absolute value of either of them.

A simple analytic treatment is instructive. To illustrate the low/high-pass filter mechanism, consider the case that the escape and interaction times are both power laws in energy,

$$\tau_{\rm esc} = a(E/E_0)^{\delta} \quad \text{and} \quad \tau_{\rm int} = b(E/E_0)^{\zeta}. \tag{3}$$

Then

$$\eta_{\rm esc}(E) = (1 + R_0(E/E_0)^{\delta-\zeta})^{-1}, \tag{4}$$

where $R_0 = a/b$ is the ratio of the escape and interaction time at reference energy E_0. When $\delta > \zeta$, the source environment acts as a *low-pass filter* on the particles injected from the accelerator, leading to a cutoff in the

escaping spectrum at high energies. This situation is typical of leaky box models of diffuse acceleration at time-independent shocks [39–41] where $\delta > 0$ because the higher the energy of the particle, the longer it needs to stay in the accelerator to reach its energy. By contrast, if the escape time decreases with energy, as in the case of diffusion in turbulent magnetic fields outside the accelerator, then it is possible to have $\delta < \zeta$ leading to a *high-pass filter* on the energy spectrum of injected nuclei: the lower the energy, the more time the nuclei have to interact before escaping, leading to a hardening of the spectrum and lightening of the composition of nuclei escaping the region surrounding the source. The spallated nucleons have energies of $E = E_A/A$; these nucleons are most abundant at low energies and have a steeper spectrum $\propto (1 - \eta_{\rm esc}(E^* A'))$. Thus the high-pass scenario leads naturally to an ankle-like feature separating the nucleonic fragments from the remaining nuclei. The normalization and slope of the spectrum of spallated nucleons relative to that of the primary nuclei is determined by how thoroughly the primary nuclei are disintegrated, which is governed by the ratio of escape and interaction lengths of the most abundant primaries.

To obtain a more realistic treatment of the interaction time, we must specify the shape of the spectrum of the target photons. In our work to date we have considered: (i) a broken power-law (BPL), characterized by its peak energy ϵ_0 and lower and upper spectral indices α, β (this is a simplified representative of nonthermal emission that allows for analytic calculation as discussed below and in Appendix B); (ii) a black-body spectrum; (iii) two types of modified black-body spectrum, which result from a reprocessed black-body in a dusty environment [42]. Details are given in Appendix A. For such peaky photon spectra the interaction time does not have the simple representation of (3) but it does have a rather universal structure. In our actual calculations we adopt a numerical integration of TALYS [43,44] and SOPHIA [46] cross sections using [47], but the analytic expression for $\tau_{\rm int}$ derived in Appendix B for the BPL in the narrow-width approximation for the interaction cross sections, is qualitatively similar and useful for understanding. As can be seen in Fig. 2 the folding of a single resonance with a broken power-law spectrum leads to a "V" shape curve for $\tau_{\rm int}$ in a log-log plot for both photo-disintegration (top panel) and photopion production (middle panel). Combining both processes in narrow-resonance approximation yields an interaction time with a "W" shape, while numerical integration including the plateau for multipion production softens the "W" to what we shall refer to as an "L" shape for brevity, a shown in the bottom panel of Fig. 2. As evident from Fig. 2, below the inflection point for photodisintegration E_b, the narrow-resonance approximation is good, while from the full numerical integration in the high-energy region $\tau_{\rm int}$ is roughly constant, so using the BPL spectrum, we have the approximate representation:

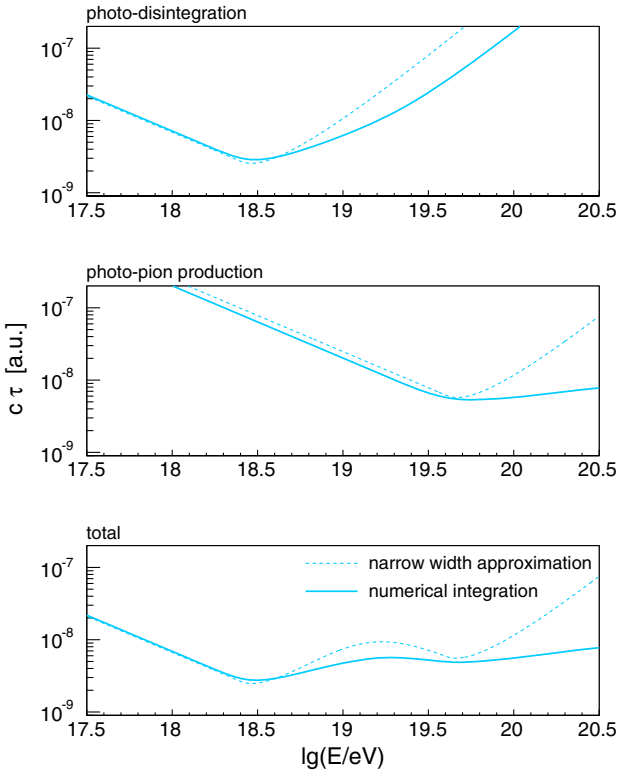

FIG. 2 (color online). Interaction times of ^{28}Si in a broken power-law photon field with parameters $\alpha = \frac{3}{2}$, $\beta = -1$ and $\epsilon_0 = 0.11$ eV. Top panel: photo-disintegration, middle panel: photo-pion production, bottom panel: sum of the two processes. The results of numerical integration using detailed cross sections are shown as thick solid lines, while those of the narrow-resonance-approximation (detailed in Appendix B) are displayed with thin dashed lines.

$$\tau_{\rm int}(E) \approx \tau_b \begin{cases} (E/E_b)^{\beta+1} & E \le E_b \\ 1 & E > E_b \end{cases}, \tag{5}$$

where formulae for τ_b and E_b are given in Appendix B, and the parameter values for photodisintegration are to be used.

Returning to the discussion of $\tau_{\rm int}$ in (3) with (5) yields the fraction of nuclei which escape without interaction in a peaky photon spectrum. It is straightforward to see that if $\delta < 0$ and the interaction time is described by an L-shaped curve, then $\eta_{\rm esc}$ has the properties of a high-pass filter. These conclusions do not depend on the exact shape of the photon spectrum. As can be seen in Fig. 13 of Appendix A, the interaction times flatten to an L-curve as well if the photon density is assumed to follow a (modified) black body spectrum.

III. COMPARISON WITH EXPERIMENT

A. Fiducial model

As our fiducial example, we adopt a broken power-law photon spectrum as a simplified representative of non-thermal emission given by

$$n(\varepsilon) = n_0^{\rm BPL} \begin{cases} (\varepsilon/\varepsilon_0)^{\alpha} & \varepsilon < \varepsilon_0 \\ (\varepsilon/\varepsilon_0)^{\beta} & \text{otherwise,} \end{cases} \quad (6)$$

where ε is the photon energy, the maximum photon number density is at an energy of ε_0 and following [39] we take the slope parameters $\alpha = +\frac{3}{2}$ and $\beta = -2$. As we shall see later, any peaky spectrum gives similar results, with the position of the peak, ε_0, being the most important parameter besides the peak photon density.

Inspired by the energy dependence of the diffusion coefficient for propagation in a turbulent magnetic field, we model $\tau_{\rm esc}$ as a power law in rigidity E/Z,

$$\tau_{\rm esc} = \tau_0 (EZ^{-1}/E_0)^{\delta}. \quad (7)$$

Since only the ratio of escape and interaction times matters, and the $\{E, A, Z\}$ dependence of this ratio is entirely determined once the spectral index of the escape time δ is specified, the remaining freedom in characterizing the source environment can be encoded by specifying the ratio of escape to interaction time for a particular choice of $\{E, A, Z\}$, which we take at 10^{19} eV for iron nuclei, denoted $R_{19}^{\rm Fe}$. In application to a particular source candidate, $R_{19}^{\rm Fe}$ depends on the density of photons and the properties of the turbulent magnetic field that delays the escape of the UHECRs from the environment of their source.

Figure 3, upper panel, shows the escape and interaction times in the fiducial source environment, as a function of the cosmic ray energy, for proton, He, N, Si and Fe; the interaction times are calculated including both photo-disintegration and photo-pion production. The gross features of the energy dependence of the interaction times can be understood in the approximation of resonant interactions in the nucleus rest frame $\varepsilon'_{\rm res}$. At low cosmic-ray energies, reaching $\varepsilon'_{\rm res}$ requires high photon energy ($\varepsilon > \varepsilon_0$), so that the interaction time decreases with increasing cosmic-ray energy as $\tau \propto E^{\beta+1}$. However for high enough cosmic ray energy, the resonance can be reached in collisions with photons of $\varepsilon < \varepsilon_0$. From here, as the cosmic ray energy increases, the photon density at the resonant energy decreases as ε^{α}, and correspondingly the interaction times increase. The laboratory energy of the inflection point of the interaction times for a cosmic ray nucleus of mass Am_p is at $E = Am_p\varepsilon'_{\rm res}/(2\varepsilon_0)$. The inflection point of the photo-dissociation times can be seen as a dip in the plot in the upper panel of Fig. 3, e.g., at around $10^{18.8}$ eV for iron nuclei. At slightly higher energy, photo-pion production becomes important, with the result that the energy dependence of the interaction time is roughly speaking an L-shaped curve in a log-log presentation.

Using these energy-dependent interaction and escape times, we propagate nuclei through the source environment with the procedure described in Appendix C. Cosmic rays of some given composition are injected from the accelerator

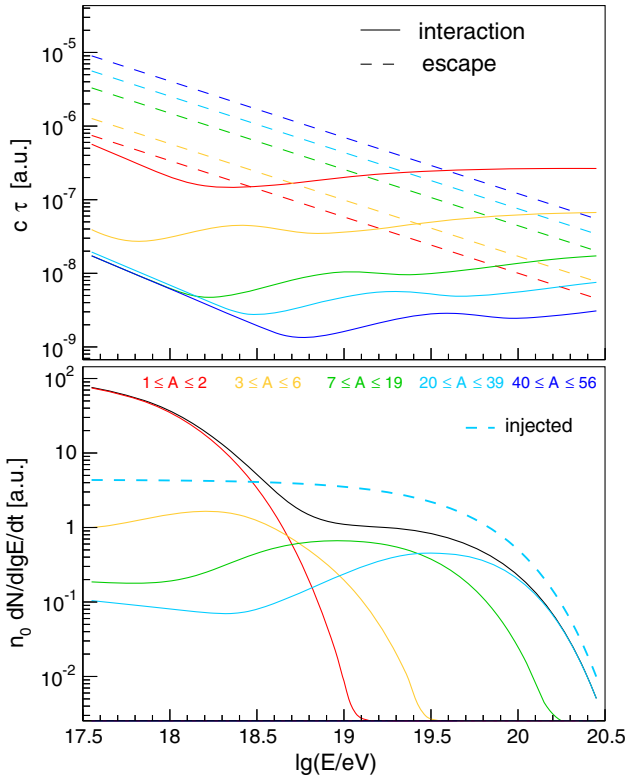

FIG. 3 (color online). Top: Interaction and escape times for $A = 1$, 4, 14, 28 and 56 (bottom to top for escape; vice versa for interaction) for the fiducial model photon field with $\varepsilon_0 = 0.11$ eV. Bottom: Injected ^{28}Si flux (bold dashed) and escaping fluxes: thin black solid line denotes the sum of all escaping nuclei and solid curves give contribution of different mass groups with low energy intercept increasing with mass. Nucleons from photo-dissociation and photo-pion-production are shown with thin-dashed and dotted curves, respectively.

into the source environment with a power law spectrum and an exponential cutoff at some maximum rigidity. To keep the complexity of the fiducial model to a minimum, we inject only a single nuclear species and fix the injection spectral index $\gamma = -1$, as expected for acceleration in young neutron stars [48]. The particles escaping the source environment are then propagated through the intergalactic medium using the procedure explained in Appendix D.

In total the fiducial model has 14 parameters, with 8 parameters allowed to float freely in the fit, as indicated in Table I. The spectral index and normalization of the Galactic spectrum are free "nuisance" parameters with the best fit giving a spectral index of −4.2. This should be understood as an effective spectral index describing the cutoff of the Galactic cosmic ray population, and hence cannot be directly compared with the parameter reported by the KASCADE-Grande Collaboration [49], because their single-power law fit is driven by the "low-energy" data. The fraction of Galactic cosmic rays at $10^{17.5}$ eV is 55%.

TABLE I. Parameters of the fiducial model. Values in brackets denote the parameters of the best-fit obtained when shifting the data by its systematic uncertainties (see text).

source parameters			
power law index of injected nuclei	γ	fix	-1
mass number of injected nuclei	A	free	28 (29)
maximum energy	$E^p_{\rm max}$	free	$10^{18.5(18.6)}$ eV
cosmic ray power density, $E > 10^{17.5}$ eV	$\dot{\epsilon}_{17.5}$	free	$9.2(13) \times 10^{44}$ erg Mpc^{-3} yr^{-1}
evolution	$\xi(z(t))$	fix	star formation rate [50]
source environment			
energy of maximum of photon field density	ε_0	free	0.11(0.07) eV
power law index of photon spectrum ($\varepsilon < \varepsilon_0$)	α	fix	$+\frac{3}{2}$
power law index of photon spectrum ($\varepsilon \geq \varepsilon_0$)	β	fix	-2
power law index of escape length	δ	free	-0.77 (-0.94)
ratio of interaction and escape time	$R^{\rm Fe}_{19}$	free	$4.4(3.7) \times 10^2$
propagation to Earth			
infrared photon background	–	fix	Gilmore12 [51]
spectrum of Galactic cosmic rays			
power law index at Earth	$\gamma_{\rm gal}$	free	-4.2 (-3.7)
mass number of Galactic nuclei	$A_{\rm gal}$	fix	56
flux fraction at $10^{17.5}$ eV	$f_{\rm gal}$	free	57 (72) %

The best description of the data is obtained with ^{28}Si of maximum energy $Z10^{18.5}$ eV $= 4.6 \times 10^{19}$ eV; the impact of allowing other parameters to vary is discussed in following sections. Normalizing this model to the observed flux at Earth, we infer a comoving volumetric energy injection rate in CRs at $z = 0$, above $10^{17.5}$ eV, of $\dot{\epsilon}_{17.5} = 9.2 \times 10^{44}$erg Mpc^{-3} yr^{-1}.

The unmodified injection spectrum and the spectrum of escaping nuclei for this fiducial model are shown in the lower panel of Fig. 3. At low energies, the nuclei are depleted relative to the injected flux because $\tau_{\rm esc} \gg \tau_{\rm int}$, but the escaping nuclei follow the original spectral index because in this example the interaction and escape times are parallel, as to be expected for $\delta = \beta + 1$. Once the corner of the L-shape is reached, the fraction of escaping nuclei grows, leading to an apparent hardening of the spectral index.

Even for the simple case in which a single nuclear species is injected into the source environment, we obtain a complex evolution of the mass composition with energy. At low energies the composition is dominated by knock-off nucleons whereas at high energies the composition becomes heavier as the ratio of escape to interaction time drops and more heavy nuclei can escape before interacting.

This fiducial model of interactions in the source environment is a very simple one, yet even so it offers a remarkably good accounting for the flux and composition at Earth as determined by the Pierre Auger Observatory. (Data from the Telescope Array (TA) are consistent with the Auger results within systematic and statistical uncertainties [52,53] and also can be well-fit; we come to TA separately below.) In Fig. 4 we compare the fiducial model prediction to the Auger measured flux, from $10^{17.5}$ eV to above 10^{20} eV [54] and to the mean and variance of the distribution of the logarithm of mass on top of the atmosphere, $\langle \ln A \rangle$ and $V(\ln A)$ [16,55,56]. There is a good overall agreement between the model and the data. The shape of the spectrum is described well, including the ankle and the flux suppression. The model also qualitatively reproduces the increase of the average logarithmic mass with energy and the decrease of its variance.

The neutrino signals of the fiducial model are shown in Fig. 5; details of the calculation are given in Appendix E. An exciting aspect of our model for the ankle is the presence of a detectable anti-electron-neutrino flux from neutron β-decay, with a rate consistent with the naïve estimate of [57]. The right panel of Fig. 5 shows the number of events as a function of energy predicted in ten years of IC86, using the IceCube acceptance for different neutrino flavors given in [58]. In total, the fiducial model predicts 3.5 events in the range 10^{16}–10^{17} eV after 10 years of operation of IceCube (corresponding to about one year of operation for an upgraded IceCube-Gen2 detector [59]). We emphasize the distinctive $\bar{\nu}_e$ enrichment due to beta decay of spallated neutrons.

The associated photon flux from nuclear deexcitation in our model is well below the Fermi-LAT data (see Appendix E for more detail). Photo-pion interactions at the source and during propagation produce an additional flux of photons via π^0-decay; this is consistent with Fermi-LAT data, as follows: If the origin of the photons measured by Fermi-LAT is exclusively from these interactions, then from [61] the associated diffuse neutrino flux saturates the IceCube upper limit [58]. Since the neutrino flux in the

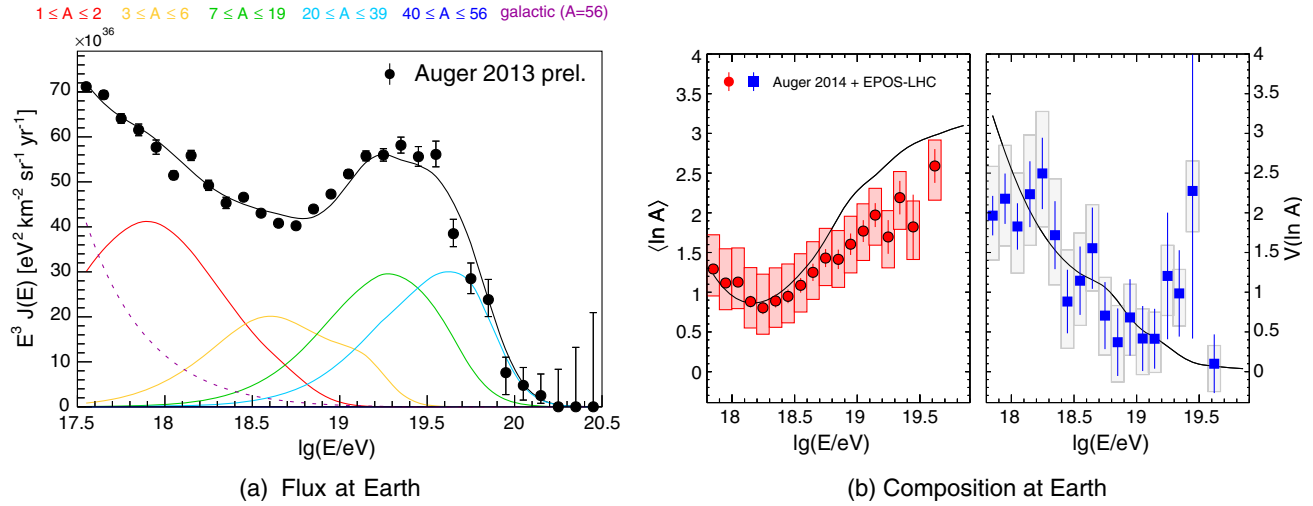

FIG. 4 (color online). Spectrum and composition at Earth. The data points are from the Pierre Auger Observatory [16,54], error bars denote the statistical uncertainties and the shaded boxes illustrate the experimental systematic uncertainties of the composition. The composition estimates are based on an interpretation of air shower data with EPOS-LHC; the lines denote the predictions of our fiducial model.

fiducial model is below the IceCube limit, it follows that also the associated photon flux is consistent with Fermi-LAT data. A more sophisticated realization of our mechanism than in the fiducial model must also respect the IceCube limits, and therefore the Fermi-LAT data as well.

B. Model variations

In this section we discuss the impact of theoretical and experimental uncertainties on our model, as well as different choices for the fiducial parameters.

1. Experimental uncertainties

To study the influence of the experimental systematic uncertainties on our fit, we have repeated the fit for all combinations of altering the measurements by $+1$, $+0$ and $-1\sigma_{\rm sys}$. of the quoted uncertainties on the energy and composition scale. We find that the best fit is obtained within the experimental systematics when shifting the energy scale up by $+1\sigma_{\rm sys} = +15\%$ and by shifting $\langle \ln A \rangle$ and $V(\ln A)$ corresponding to a shift of the shower maximum by $-1\sigma_{\rm sys} \approx -10$ g/cm^2. The best-fit values after the application of these shifts are shown in brackets in Table I. Most notably, the peak energy of the photon spectrum decreases from 110 to 70 meV and the best-fit value of the spectral index of the escape time decreases from $\sim -3/4$ to almost -1. The neutrino flux at Earth obtained for this fit is about 30% smaller than in case of the fiducial model. This is mainly due to the difference in the

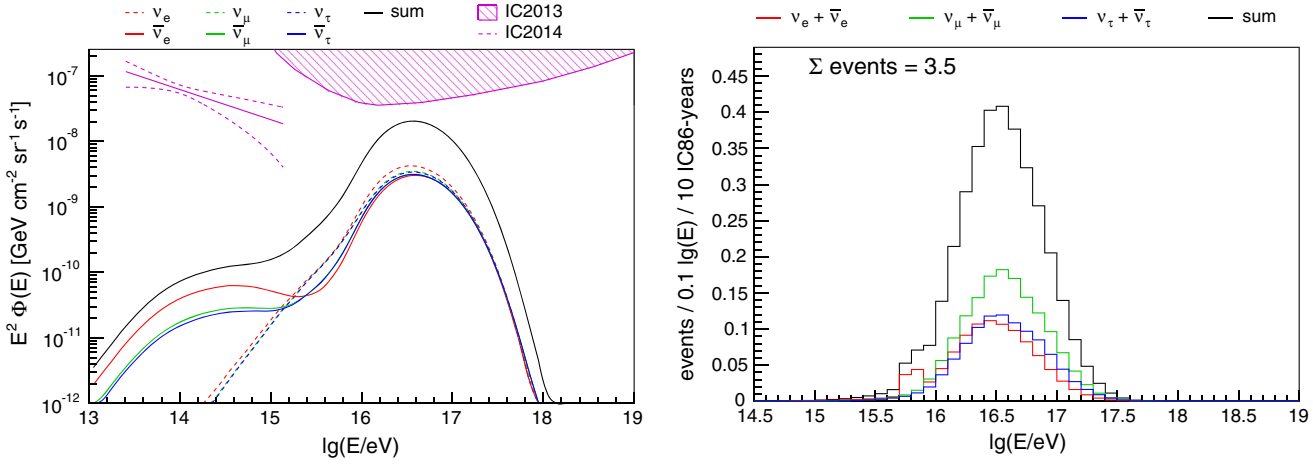

FIG. 5 (color online). Neutrino spectrum (left) and expected number of events in 10 IC86-years (right) for the fiducial model. The measured flux of low-energy extragalactic neutrinos from IceCube [60] is shown in the left panel (purple lines) as well as the 90% CL upper limit on the flux of high-energy neutrinos (dashed area) [58]. The peak in the electron neutrino flux at about $10^{15.8}$ eV seen in the right panel is due to the increased interaction probability of anti-electron neutrinos at the Glashow resonance.

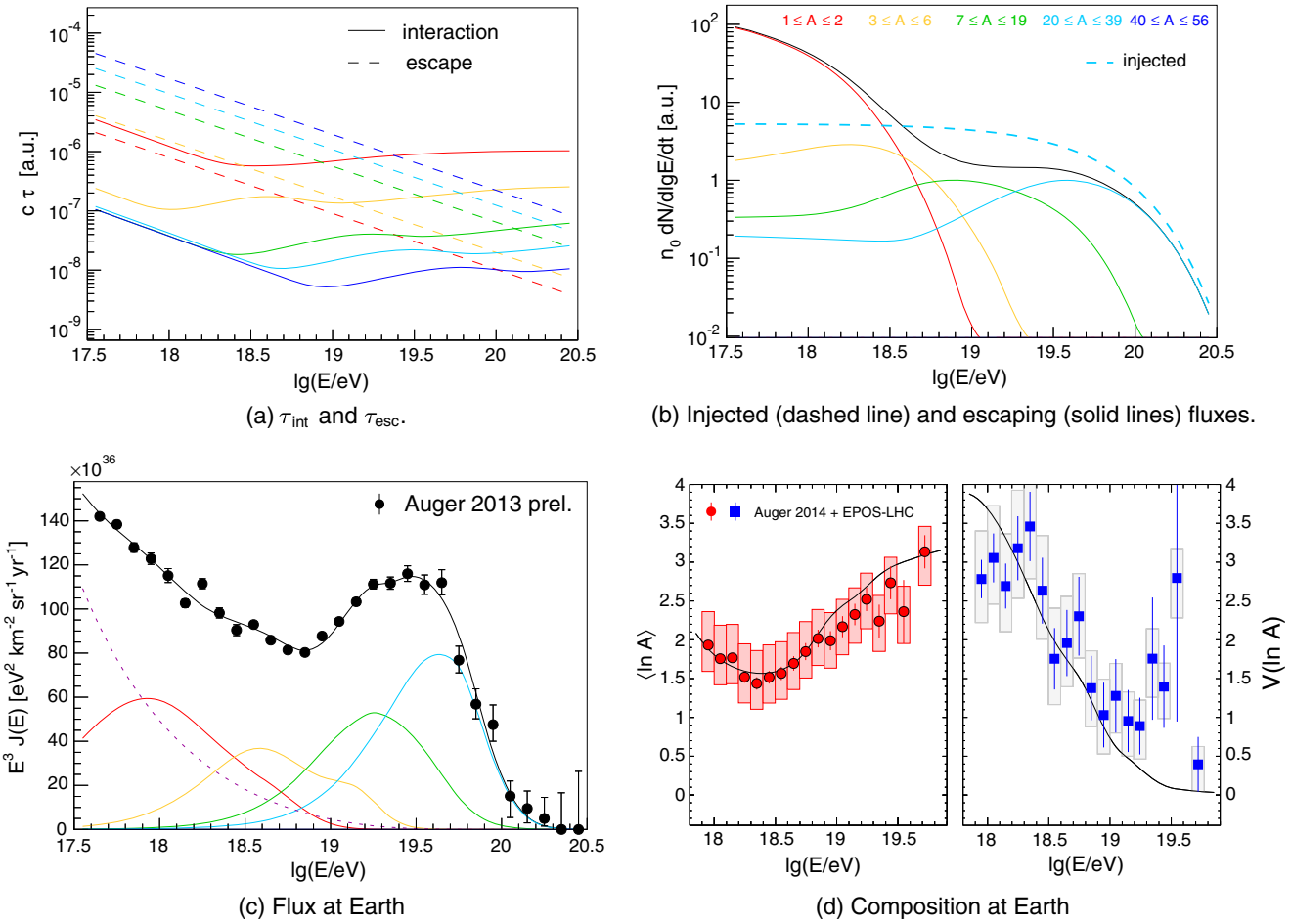

FIG. 6 (color online). Spectrum and composition at Earth. The data points are from the Pierre Auger Observatory [16,54] shifted by plus one sigma of systematic uncertainty for the energy scale and minus one sigma for the X_{max} *scale*. The lines denote the best-fit within our fiducial model.

best-fit peak energy of the photon field in the source environment. The sensitivity of the neutrino flux to ε_0 will be further discussed in Sec. III B 5.

The overall description of the spectrum and composition is considerably improved, as can be seen in Fig. 6. The model variations discussed below will therefore be performed based on shifted data.

2. Hadronic interactions in air showers

The interpretation of experimental air shower data in terms of mass composition relies on the validity of extrapolations of the properties of hadronic interactions to ultrahigh energies. Using alternative models for this interpretation (SIBYLL2.1 [62] or QGSJETII-04 [63] instead of EPOS-LHC [64]), decreases the value of the $\langle \ln A \rangle$ data points by about $\langle \ln A \rangle = -0.6$ and leads to a worse fit of the data. If this difference between models gives a fair estimate of the uncertainties of the mass determination in both directions, $\sigma_{\text{theo}}(\langle \ln A \rangle) = \pm 0.6$, then a hadronic interaction model that leads to a heavier interpretation of Auger data than EPOS-LHC would make the fit with the fiducial model even better, similar to the systematic shift in the composition scale discussed in the previous section.

3. Mass composition at the source

It is remarkable that a good description of both the spectrum and mass composition at Earth is possible by assuming only a single injected species at the source as assumed for simplicity in the fiducial model. However, depending on the astrophysical scenario, this might be an unrealistic assumption.

In Fig. 7 we explore the capability of our model to incorporate additional flux components of mass A_1 below and above the mass $A_2 \sim 29$ that gives the best fit for the fiducial single-mass model. As can be seen, our calculation allows for an additional proton or helium component as large as 80% and up to 70% for nitrogen.

For an additional flux component with a heavy mass, the model is more restrictive as illustrated in the lower left panel of Fig. 7 using $A_1 = 56$. In this case, the description of the data considerably deteriorates for fractions above 10%. The reason for this behavior is twofold. First, the injection of too much iron at the source leads to a too heavy

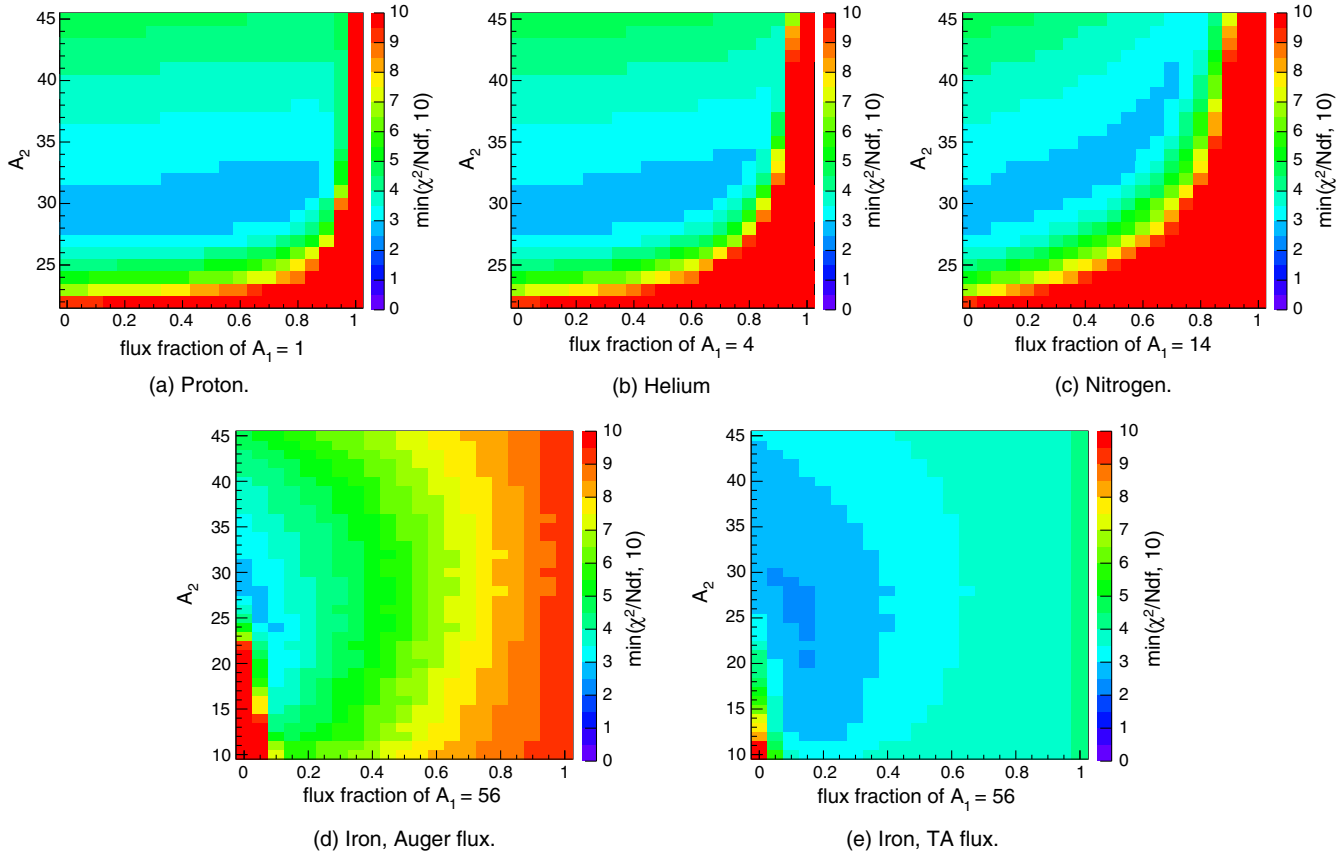

FIG. 7 (color online). Injection of two mass components. The first mass value, A_1, is fixed and contributes the fraction indicated on the x-axis to the total flux. The second mass value, A_2, is varied as shown on the y-axis. The fit quality is indicated by the colors.

composition at Earth as compared to the estimates from the Pierre Auger Observatory. Second, if the end of the cosmic ray spectrum is to be described by the maximum rigidity of iron nuclei, then the energy of secondary nucleons needed to populate the flux at and below the ankle is too small to describe the data (the maximum energy of secondary nucleons is $1/A$ of the maximum energy of nuclei).

If the cutoff of the flux is at higher energies, as suggested by the measurement of TA [65], then a larger fraction of iron primaries at the source can be incorporated, as shown in the lower right panel of Fig. 7. When using the TA data in the fit, as shown in Fig. 8, the spectrum can be described reasonably well even for an injected flux consisting of 100% iron nuclei. But in this scenario the composition at Earth at ultrahigh energies is heavier than suggested by the interpretation of the $X_{\max}$ data of Auger.

As an illustration of a more complex composition model, we use the abundances of Galactic nuclei at a nucleus energy of 1 TeV, which we read from Fig. 28.1 in [66]. The flux fractions are 0.365, 0.309, 0.044, 0.077, 0.019, 0.039, 0.039, 0.0096, 0.014, 0.084 for H, He, C, O,Ne, Mg, Si, S, Ar + Ca, Fe, respectively. The resulting fit is shown in Fig. 9 ($\gamma = -1.25$ and $\delta = -1$). This example demonstrates that our mechanism for producing the ankle is working even when considering a complicated mix of primaries.

4. Source evolution and spectral index

To have a concrete fiducial model, we needed to specify how the production of UHECRs varied over cosmological time scales. This is known as the source evolution, which we took to be in direct proportion to the star-formation-rate—as would be expected in a source scenario such as young magnetars. In this section, we consider alternative evolutions of the source luminosity density described by the simple one-parameter functional form

$$\xi(z) = \begin{cases} (1+z)^m & z < z_0 \\ (1+z_0)^m \exp\left(-(z-z_0)\right) & \text{otherwise} \end{cases} \quad (8)$$

with $z_0 = 2$ and m ranging from -4 to $+4$. $m = 0$ yields a uniform source luminosity distribution, $m = +4$ corresponds to a strong evolution similar to the one of active galactic nuclei, and negative values result in sources that are most abundant or most luminous within the low-redshift universe as suggested in [67]. The resulting fit parameters are displayed in Fig. 10 for three choices of the spectral index γ of the injected flux: -1, as in the fiducial model, -2 as expected for stochastic shock acceleration and for letting γ float freely in the fit. As can be seen in Fig. 10(a), $\gamma = -2$ gives a poor description of the data for $m \gtrsim 0$, but is a

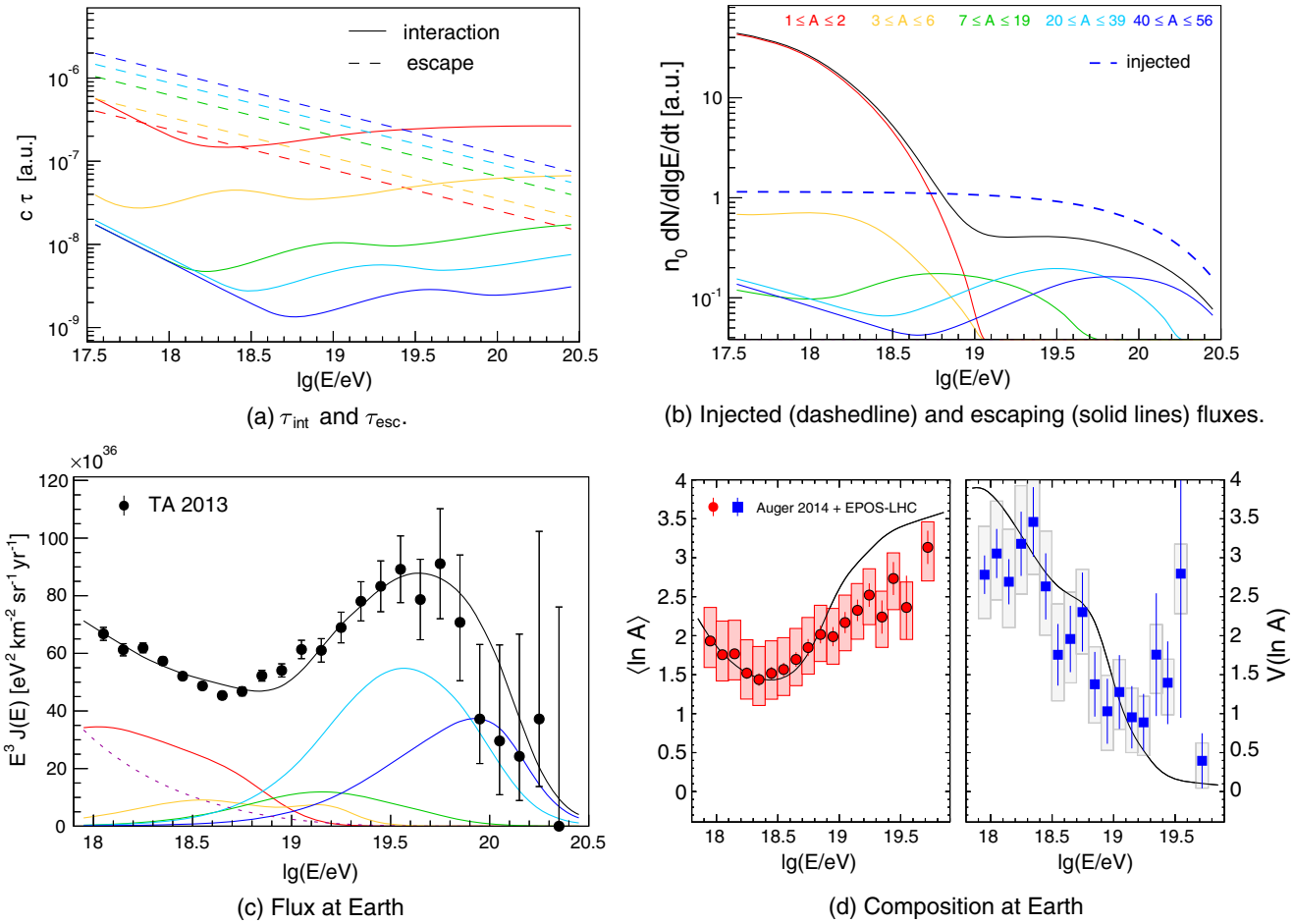

FIG. 8 (color online). Spectrum and composition at Earth. The data points are from the TA [65] (flux) and the Pierre Auger Observatory [16] (composition). The latter have been shifted in energy to match the energy scale of TA and the X_{max} scale is shifted down by 1 sigma. The lines denote the fit with our model assuming a pure iron composition at the source.

viable choice for close by sources, in accordance to the findings of [67]. For positive values of m, a fixed value of $\gamma = -1$ gives a similar fit quality as the freely floating γ, but the latter converges to values larger than -1 for source evolutions with $m > 2$ [cf. Fig. 10(c)].

For the "traditional" source evolutions with $m \geq 0$ and the fit with $\gamma = -1$ we find that most of the parameters exhibit only a minor variation with m, with the exception of the power-law index of the escape time δ [Fig. 10(e)] and the power density $\dot{\epsilon}_{17.5}$ [Fig. 10(e)].

We conclude that our model for the ankle does not critically depend on the choice of the source evolution, but that for a given choice of m we can constrain the allowed values of γ, δ and $\dot{\epsilon}_{17.5}$.

5. Photon spectrum

We repeated the model fits using alternative energy distributions of the photon density instead of the broken power law used in the fiducial model: a black body spectrum and two modified black body spectra. All four spectra are normalized to the same integral photon density and depend only on one parameter, the peak energy ε_0 (see Appendix A). The resulting fit results are shown in Fig. 11 for a freely floating spectral index γ and for source evolutions with $m \geq 0$. As can be seen, all four photon spectra describe the data equally well [Fig. 11(a)]. The best-fit values of the free model parameters are very similar and in particular the obtained peak values are within ± 20 meV. We conclude that as long as the photon spectrum is "peaky," the particular details of its shape do not influence the parameters of our model.

The sensitivity of the fit to the peak energy is shown in the left panel of Fig. 12. As can be seen, the χ^2 deteriorates very quickly at low values of ε_0, but it is almost flat above the minimum. This feature can be easily understood recalling ε_0 in the "L-curve" approximation introduced in Sec. II: The smaller ε_0, the larger is the energy of inflection of the interaction length, E_b. For too-small values of ε_0, the interaction and escape times are parallel over the full energy range and thus no high-pass filter is created. On the other hand, once E_b is small enough, a further decrease changes only the flux at low energy, where the escaping

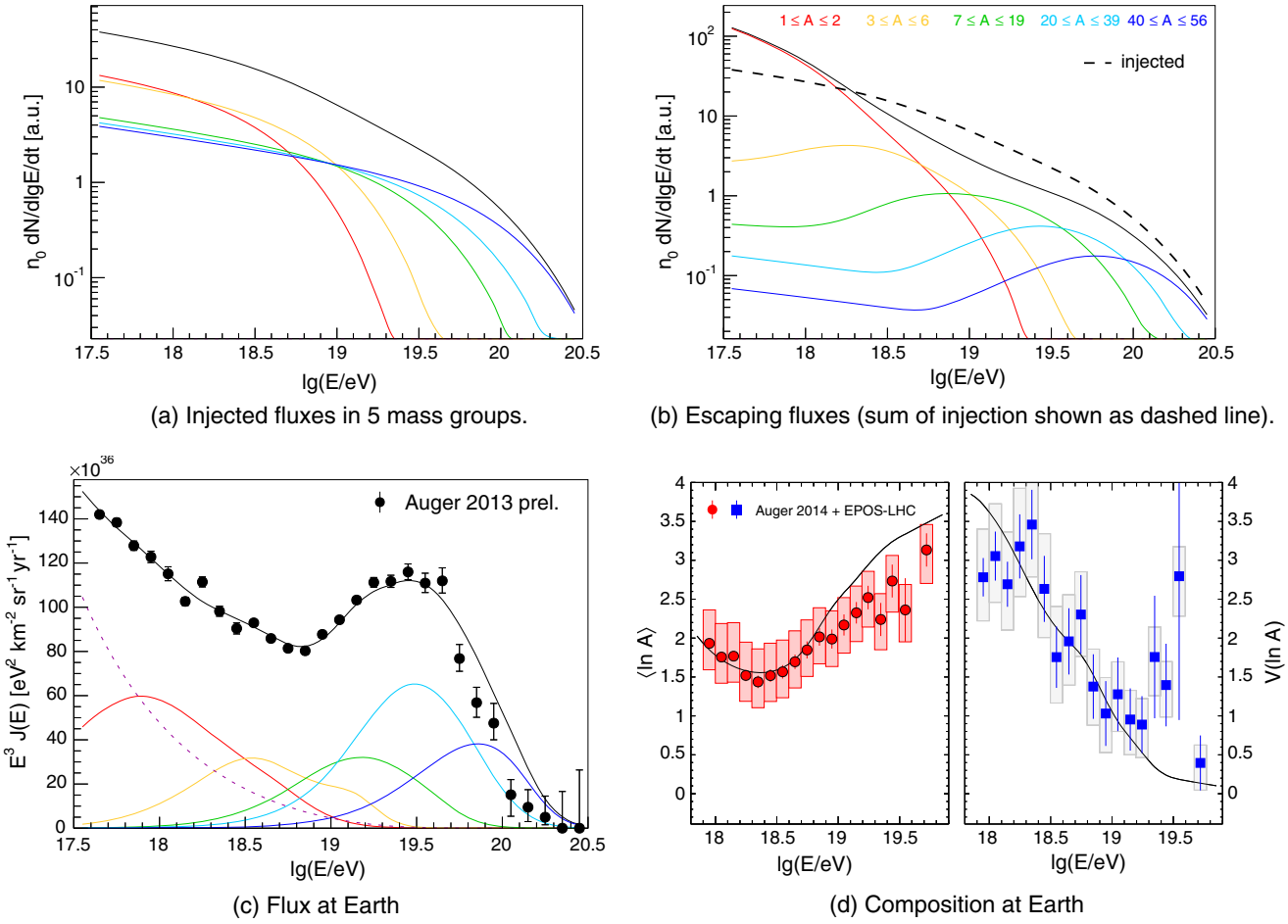

FIG. 9 (color online). Spectrum and composition at Earth. The data points are from the Pierre Auger Observatory [16,54] shifted by their systematic uncertainty as in Fig. 6. The injected composition follows a Galactic mixture with 10 elements (see text).

spectrum is dominated by low-mass nuclei from spallation (see e.g. Fig. 3) which can be compensated by adjusting other parameters such as R_{19}^{Fe}.

To first order, our model can therefore only give a lower limit on the peak energy of the photon flux in the source environment. However, future limits or observations of neutrinos in the 10–100 Pev range will help to constrain this important source property, because the number of predicted neutrinos strongly depends on ε_0, as shown in the left panel of Fig. 12 by the superimposed open symbols. A larger peak energy of the ambient photon environment increases neutrino production at the source in two ways. First, shifting E_b to lower energies (and compensating as necessary by adjustment of R_{19}) moves the interaction times of protons closer to the escape time and correspondingly additional neutrinos are produced via photo-pion production of protons (compare e.g. the red curves at around 10^{18} eV in the upper panel of Fig. 3 ($\varepsilon_0 = 110$ meV) to the ones in Fig. 6(a) [$\varepsilon_0 = 70$ meV)]. Second, increasing ε_0 moves the minimum of the interaction time for photo-pion production of nuclei to lower energies. Since the neutrinos from photo-pion production carry a larger fraction of the nucleon energy than the neutrinos from neutron decay after photo-dissociation, this increases the neutrino flux as well.

It is tempting to give a quantitative interpretation of the χ^2-curve of Fig. 12 in terms of a lower limit on ε_0 and the number of neutrinos. However, the minimum of χ^2 is far away from $\chi^2/N_{\mathrm{df}} = 1$ which—assuming this model is correct—is indicative of experimental systematics or an underestimation of the experimental uncertainties or of deficiencies in the modeling of hadronic interactions in the atmosphere needed to interpret the data in terms of mass composition (see above). In the absence of a concrete explanation we follow the PDG [66,68] and rescale the uncertainties by a common factor $S = (\chi^2_{\mathrm{min}}/N_{\mathrm{df}})^{\frac{1}{2}}$ to bring the rescaled χ^2/N_{df} to 1. This rescales the χ^2 value of any given model so that the number of standard-deviations it is from the minimum is given by $N'_\sigma = S^{-1}\sqrt{\chi^2_{\mathrm{model}} - \chi^2_{\mathrm{min}}}$. This yields an approximate lower limit on ε_0 at $N'_\sigma = 3$ of $\varepsilon_0 > 34$ meV and $N_\nu(10 \times \mathrm{IC86}) > 0.4$ assuming the validity of the fixed fiducial parameters given in Table I. The corresponding lower temperature limits are 180 K, 125 K and 100 K for the black body spectra with $\sigma = 0$, 1 and 2

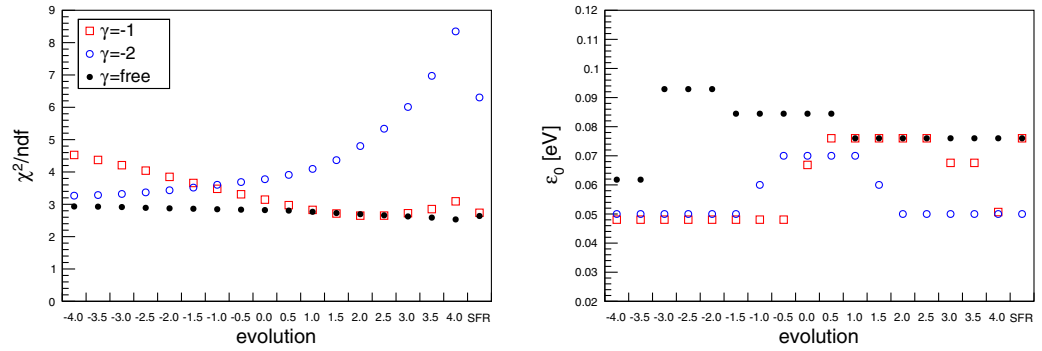

(a) fit quality.

(b) peak energy.

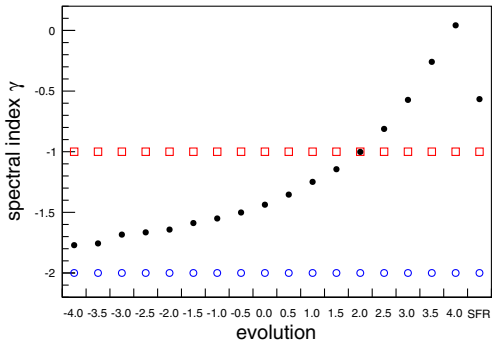

(c) spectral index of injected spectrum.

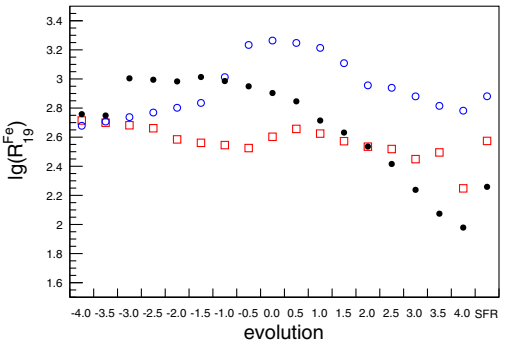

(d) ratio of escape and interaction time.

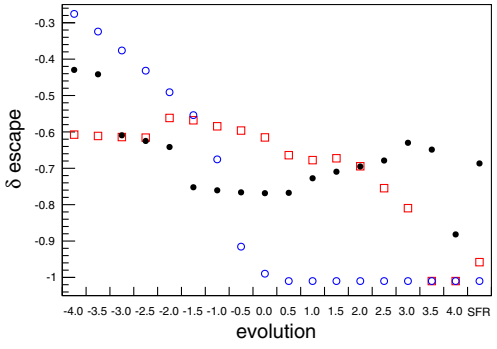

(e) power-law index of escape time.

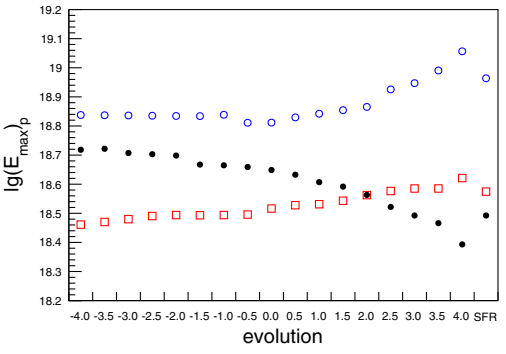

(f) maximum energy for $Z = 1$.

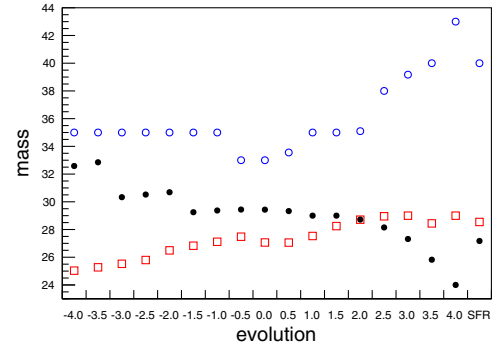

(g) injected mass

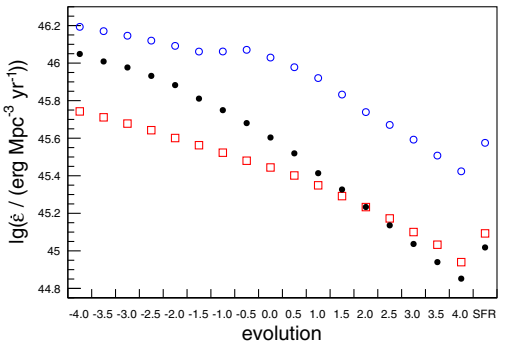

(h) UHECR energy injection rate

FIG. 10 (color online). Fit results as a function of source evolution for different spectral indices of the injected flux: γ fixed to -1 (open squares), fixed to -2 (open circles) and best fit (filled circles). On the x-axis the power m of the source evolution is shown; the last bin reports the values for the fiducial model (SFR) evolution from [50], Eq. (D6).

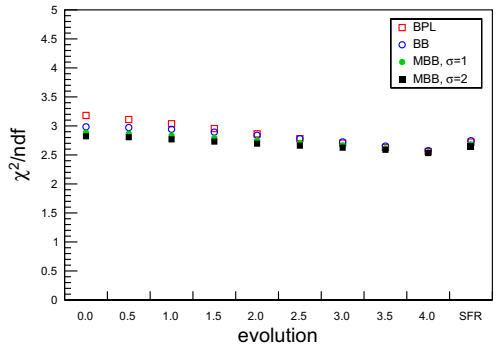

(a) fit quality.

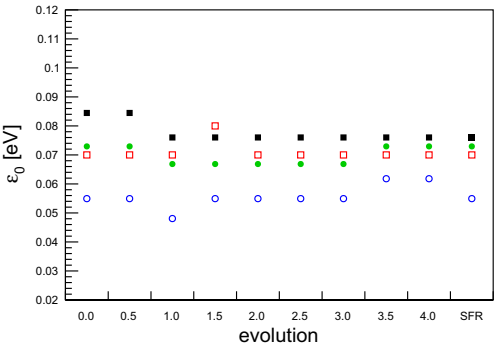

(b) peak energy.

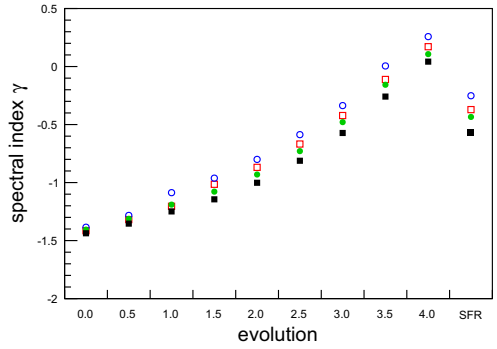

(c) spectral index of injected spectrum.

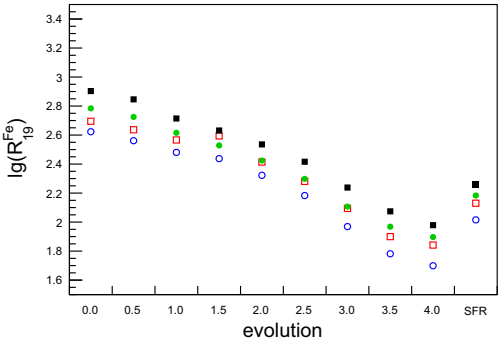

(d) ratio of escape and interaction time.

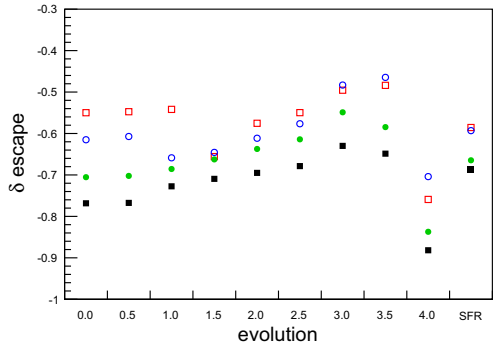

(e) power law index of escape time.

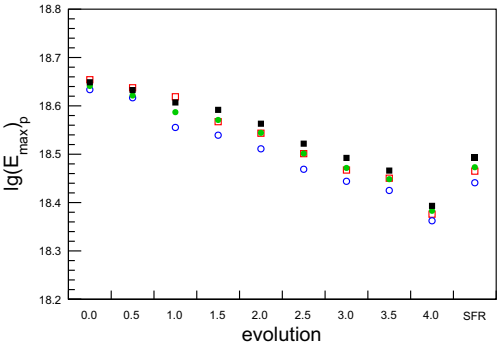

(f) maximum energy for Z " 1.

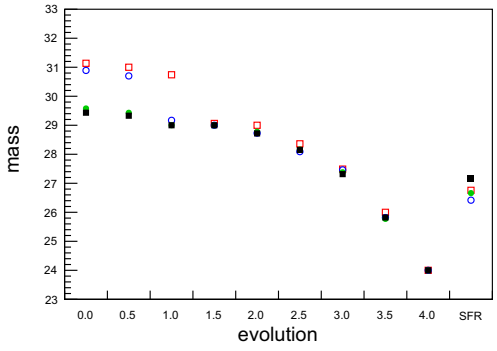

(g) injected mass

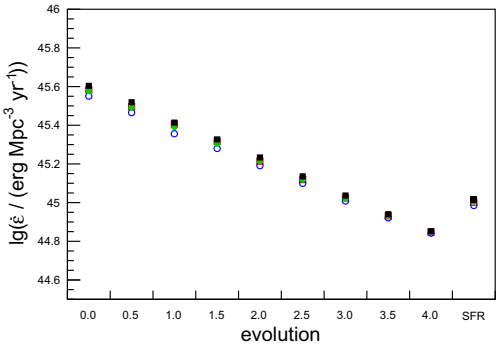

(h) UHECR energy injection rate

FIG. 11 (color online). Fit results as a function of source evolution for different photon spectra: Broken power law (BPL, open squares), black body spectrum (BB, open circles), modified black body spectrum (MBB) with $\sigma = 1$ (filled circles) and $\sigma = 2$ (filled squares). On the x-axis the power m of the source evolution is shown and in the last bin the fit values for the fiducial evolution from [50], Eq. (D6), is shown.

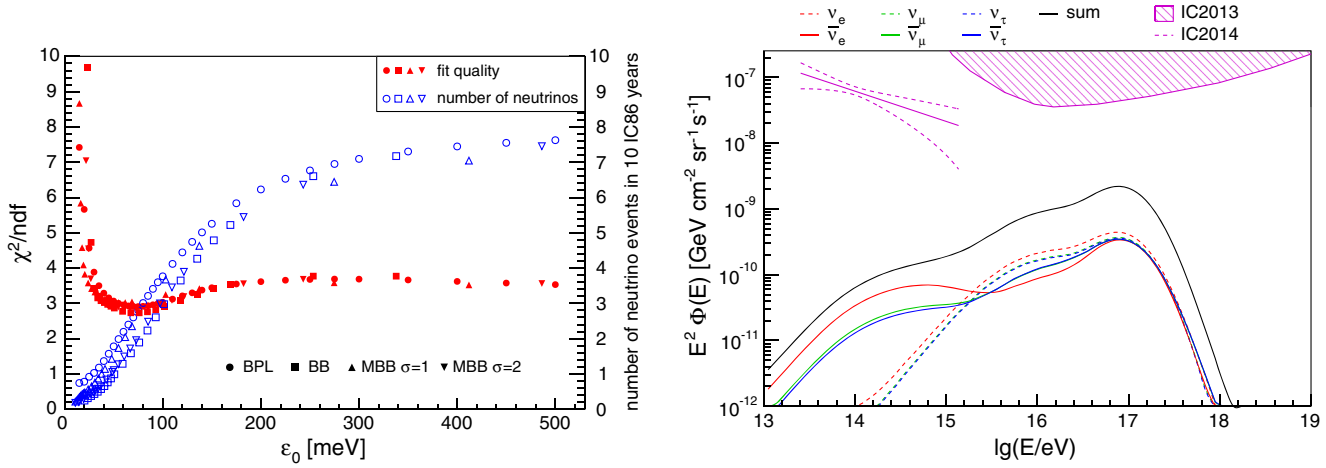

FIG. 12 (color online). Left: Fit quality of the fiducial model (closed symbols) and number of neutrinos (open symbols) as a function of peak energy ε_0 of the photon spectrum in the source environment. Four types of photon spectra are shown: Broken power law (BPL), black body spectrum (BB) and two modified black body spectra (MBB). The minimum χ^2 of BPL corresponds to the result shown in Fig. 6. Right: Lower limit on the neutrino flux obtained for a modified black body spectrum with $\sigma = 2$, and $\varepsilon_0 = 34$ meV ($T = 100$ K). The lines and hatched area at the top of the figure are the measured neutrino flux and upper limit from IceCube [58,60].

respectively. The lower limit on the neutrino spectrum is shown in the right panel of Fig. 12.

6. Hadronic interactions in the source environment

In addition to interactions with the background photon field, nucleons and nuclei can also scatter off hadrons in the source environment. In this paper we assume that the density of hadronic matter in the source environment is low enough that such hadronic interactions can be neglected. For any concrete astrophysical realization of our scenario, one must check and if necessary include hadronic interactions in the source environment. Production of $\pi^{\pm}$'s and π^0's in hadronic collisions could significantly increase the fluxes of neutrinos and photons emitted in the EeV energy range. Fast-spinning newborn neutron stars provide a particular example [69]. Precise estimates of the impact of hadronic collisions on the predictions of our model will be presented in a separate publication. The results presented here are valid for all astrophysical systems in which the interactions are dominated by photo-nuclear processes.

IV. CONCLUSIONS

In this paper we have proposed a new explanation for the ankle in the cosmic ray spectrum, and for the evolution with energy of the composition of extragalactic cosmic rays: from light below the ankle to increasingly heavy above. When nuclei are trapped in the turbulent magnetic field of the source environment, their escape time can decrease faster with increasing energy than does their interaction time. Under these conditions, only the highest energy particles can escape the source environment unscathed, and the source environment acts as a high-pass filter on UHECRs. Nuclei below the crossover energy such that $\tau_{\rm esc} > \tau_{\rm int}$ interact with photons in the environment around the source, with ejection of nucleons or alpha particles and consequent production of a steep spectrum of secondary nucleons. The superposition of this steeply falling nucleon spectrum with the harder spectrum of the surviving nuclear fragments creates an ankle-like feature in the total source emission spectrum. Above the ankle, the spectrum emerging from the source environment exhibits a progressive transition to heavier nuclei, as the escape of noninteracting nuclei becomes efficient. Abundant production of $\bar{\nu}_e$'s is a signature of this mechanism.

We illustrated the high quality of the fit which can be obtained to the Auger data, with a fiducial model in which nuclei are accelerated up to a maximum rigidity found to be $\approx 10^{18.5}$ V, with spectrum $\propto E^{-1}$, and are then subject to photo-disintegration in the vicinity of the accelerator before escaping for their journey to Earth. We showed that the details of the photon spectrum around the accelerator are unimportant, except for its peak energy. The other important characteristic of the environment is the photon density relative to the magnetic diffusivity, which we characterized in a very simplistic way (through a single parameter) in this initial study. We studied the sensitivity of the mechanism to the energy-scale uncertainty and hadronic-interaction-modeling uncertainty, which affects the composition inferred from the atmospheric shower observations, and also used the TA spectrum instead of the Auger spectrum. The conclusion of these studies is that a good quality fit can be obtained in most cases, but details of the fit parameters such as the composition and maximum energy characterizing the accelerator change. A corollary is that until these systematic uncertainties in the observations and their interpretation are reduced, such details of the accelerator cannot be reliably inferred from the data. The fiducial model parameters needed

in the fits are such that the scenario can be reasonably achieved in at least one type of proposed astrophysical source, as will be discussed in a future publication.

Our mechanism has two predictions beyond fitting the shape of the spectrum and composition evolution, which are independent of many environmental variables and can be used to test the validity of this scenario for production of the ankle. (i) The spectral cutoff of spallated nucleons emerging from the source environment is $\frac{1}{2}R_{\rm max}$, where $R_{\rm max}$ is the rigidity cutoff of the accelerator, because $E_{\rm max,spal\ nuc} = E_{{\rm max},A}/A$ while $E_{{\rm max},A} = ZR_{\rm max}$, and finally $Z/A = \frac{1}{2}$, largely independent of composition. This relation holds prior to the extragalactic propagation from the source, thus giving complementary information on the accelerator to that obtained from the spectrum and composition above the ankle alone. (ii) There is a one-to-one relation between the spectrum of spallated nucleons and the anti-electron-neutrinos produced by beta decay of neutrons, unless the spallated nucleons lose energy by interacting with hadronic material in the source environment. Independent of other properties of the environment or the source evolution, $\bar{\nu}_e$'s will have an identical spectral shape, shifted down by a factor $\sim 1/1000$ from the kinematics of $n \to pe^-\bar{\nu}_e$ and reduced by a factor-2 in normalization because only half the nucleons are neutrons. This follows because propagation energy losses are small for nucleons of such low energy, and redshift impacts both nucleons and neutrinos identically. Thus, detailed comparison of the $\bar{\nu}_e$ and spallated nucleon spectra will reveal if hadronic interactions in the source environment are important, which would imply a correlated production of photo-pion produced neutrinos.

ACKNOWLEDGMENTS

We would like to acknowledge many useful discussions with our colleagues of the Pierre Auger Collaboration. Furthermore we thank David Walz for his support regarding questions about CRPropa and Benoit Marchand for his help running the calculations on the BuTinah high performance computing cluster of NYU Abu Dhabi. M. U. acknowledges the financial support from the EU-funded Marie Curie Outgoing Fellowship, Grant PIOF-GA-2013-624803. The research of G. R. F. is supported in part by the U.S. National Science Foundation (NSF), Grant PHY-1212538 and the James Simons Foundation; she thanks KIPAC/SLAC for their hospitality. The research of LAA is supported by NSF (Grant CAREER PHY-1053663) and NASA (Grant NNX13AH52G); he thanks the Center for Cosmology and Particle Physics at New York University for its hospitality.

Note added.—After this work was presented at the IceCube Particle Astrophysics Symposium, a paper appeared on the arXiv exploring another mechanism for producing the ankle, arising in the context of gamma-ray bursts [70].

APPENDIX A: PHOTON SPECTRA

In this paper we explore the propagation effects of the four types of photon spectra shown in Fig. 13. The first consists of broken power-law (see e.g., [39]) as a simplified representative of nonthermal emission given by

$$n(\varepsilon) = n_0^{\rm BPL}\begin{cases}(\varepsilon/\varepsilon_0)^{\alpha} & \varepsilon < \varepsilon_0\\ (\varepsilon/\varepsilon_0)^{\beta} & \text{otherwise,}\end{cases} \tag{A1}$$

where ε is the photon energy and the maximum of the number density is at an energy of ε_0.

We also consider modified black-body spectra using the functional form

$$n(\varepsilon) = n_0^{\rm MBB}\frac{8\pi}{(hc)^3}\frac{\varepsilon^2}{e^{\frac{\varepsilon}{kT}}-1}\left(\frac{\varepsilon}{\varepsilon_0}\right)^{\sigma} \tag{A2}$$

where T denotes the temperature in the case of pure black-body, and the absorption factor is given by $(\frac{\varepsilon}{\varepsilon_0})^{\sigma}$ (see e.g. [42]). h, k and c are the Planck constant, Boltzmann constant and speed of light, respectively. For $\sigma = 0$ and $n_0^{\rm MBB} = 1$ the unmodified black-body spectrum is obtained. The relation between the peak energy and temperature parameter is given by a modified Wien's displacement law,

$$\varepsilon_0 = [{\rm W}(-e^{-b}b) + b]kT, \tag{A3}$$

where ${\rm W}(x)$ is the Lambert function (see e.g. [71]) and $b = \sigma + 2$.

For the study of the effect of using different functional forms of photon spectra in our model (cf. Sec. III B 5), it is useful to use a common normalization for all spectra. The integral photon density of Eq. (A1) is

$$I_{\rm BPL} = n_0^{\rm BPL}\varepsilon_0\left(\frac{1}{\alpha+1} - \frac{1}{\beta+1}\right) \tag{A4}$$

and for Eq. (A2) it is

$$I_{\rm MBB}^{\sigma} = n_0^{\rm MBB}\frac{8\pi}{(hc)^3}(kT)^3\zeta(\sigma+3,1)\Gamma(\sigma+3), \tag{A5}$$

where $\zeta(x)$ denotes the Riemann zeta function and $\Gamma(x)$ is the Gamma function. Choosing the photon density of the unmodified black body spectrum as reference we use the following normalization constants,

$$n_0^{\rm BPL} = I_{\rm MBB}^0/I_{\rm BPL} \tag{A6}$$

and

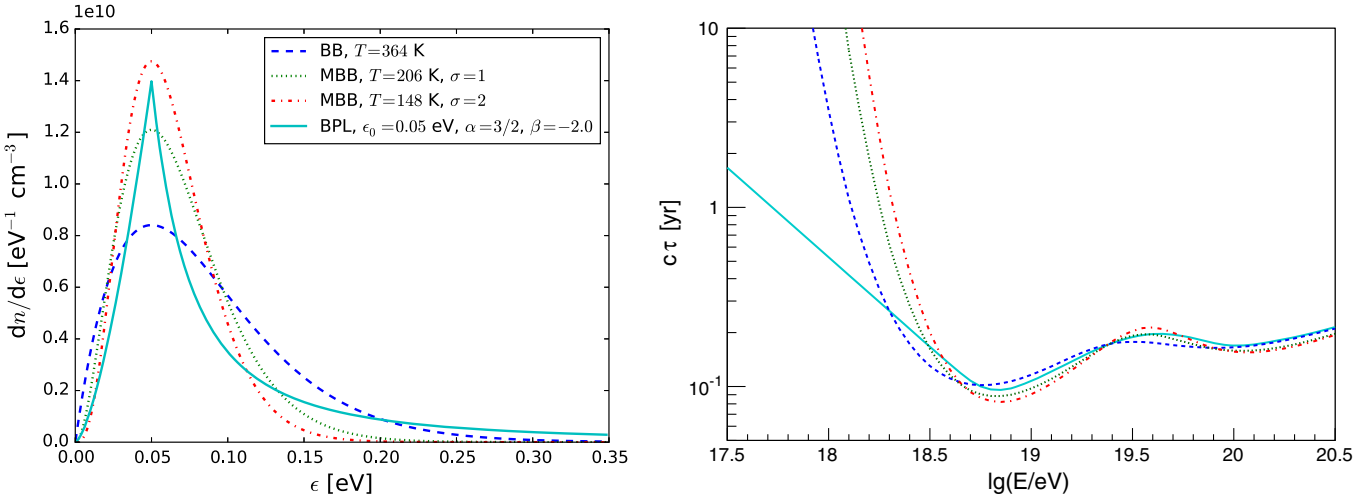

FIG. 13 (color online). Left: Comparison of photon spectra. BPL: Broken power law (solid), BB: black body spectrum (dashed), MBB: modified black body spectrum (dotted and dash-dotted). The curves are normalized to match the integral of the black body spectrum and the temperatures are chosen to match the peak energy of the broken power law. Right: Interaction times corresponding to the four photon spectra.

$$n_0^{\rm MBB}(\sigma) = I^0_{\rm MBB}/I^\sigma_{\rm MBB}. \tag{A7}$$

An example of the four photon spectra after normalization and for the same peak energy of $\varepsilon_0 = 50$ meV is shown in the left panel of Fig. 13. The corresponding interaction time for the sum of photo-dissociation and photo-pion production is shown in the right panel.

APPENDIX B: PHOTO-NUCLEAR INTERACTIONS

The interaction between photons and high energy nuclei has been extensively discussed in the literature [72–82]. In this appendix, we describe how we implement the photon-nucleus collisions in our analysis. The interaction time for a highly relativistic nucleus with energy $E = \gamma A m_p$ (where γ is the Lorentz factor) propagating through an isotropic photon background with energy ε and spectrum $n(\varepsilon)$, normalized so that the total number density of photons is $\int n(\varepsilon)d\varepsilon$, is given by [72]

$$\frac{1}{\tau_{\rm int}} = \frac{c}{2}\int_0^\infty d\varepsilon \frac{n(\varepsilon)}{\gamma^2\varepsilon^2}\int_0^{2\gamma\varepsilon} d\varepsilon'\varepsilon'\sigma(\varepsilon'), \tag{B1}$$

where $\sigma(\varepsilon')$ is the photo-nuclear interaction cross section of a nucleus of mass Am_p by a photon of energy ε' in the rest frame of the nucleus.

Detailed tables of $\sigma(\varepsilon')$ are available in CRPropa [83,84]. We use the numerical tools provided at [47] to calculate the interaction times for the photon field given by Eqs. (A1) and (A2).

For illustrative purposes, the cross section can be approximated by a single pole in the narrow-width approximation,

$$\sigma(\varepsilon') = \pi\sigma_{\rm res}\frac{\Gamma_{\rm res}}{2}\delta(\varepsilon' - \varepsilon'_{\rm res}), \tag{B2}$$

where $\sigma_{\rm res}$ is the resonance peak, $\Gamma_{\rm res}$ its width, and $\varepsilon'_{\rm res}$ the pole in the rest frame of the nucleus. The factor of $1/2$ is introduced to match the integral (i.e. total cross section) of the Breit-Wigner and the delta function [85].

The mean interaction time is obtained substituting Eq. (B2) into Eq. (B1),

$$\begin{aligned}\frac{1}{\tau_{\rm int}(E)} &\approx \frac{c\pi\sigma_{\rm res}\varepsilon'_{\rm res}\Gamma_{\rm res}}{4\gamma^2}\int_0^\infty \frac{d\varepsilon}{\varepsilon^2}n(\varepsilon)\Theta(2\gamma\varepsilon - \varepsilon'_{\rm res}) \\ &= \frac{c\pi\sigma_{\rm res}\varepsilon'_{\rm res}\Gamma_{\rm res}}{4\gamma^2}\int_{\varepsilon'_{\rm res}/2\gamma}^\infty \frac{d\varepsilon}{\varepsilon^2}n(\varepsilon).\end{aligned} \tag{B3}$$

Substituting (A1) into (B3) yields:

$$\frac{1}{\tau_{\rm int}(E)} = \frac{1}{\tau_b}\begin{cases}(E_b/E)^{\beta+1} & E \le E_b \\ (1-\beta)/(1-\alpha)[(E_b/E)^{\alpha+1} - (E_b/E)^2] + (E_b/E)^2 & E > E_b\end{cases}, \tag{B4}$$

where

$$\tau_b = \frac{2E_b(1-\beta)}{c\pi\sigma_{\rm res}Am_p\Gamma_{\rm res}n_0} \quad \text{and} \quad E_b = \frac{\varepsilon'_{\rm res}Am_p}{2\varepsilon_0}. \tag{B5}$$

The parameters characterizing the photo-disintegration cross section are: $\sigma_{\rm res} \approx 1.45 \times 10^{-27}$ cm$^2 A$, $\Gamma_{\rm res} = 8$ MeV, and $\epsilon'_{\rm res} = 42.65A^{-0.21}(0.925A^{2.433})$ MeV, for $A > 4$ ($A \leq 4$) [74]. The parameters for the photo-pion production cross section are: $\sigma_{\rm res} \simeq 5.0 \times 10^{-28}$ cm$^2 A$, $\Gamma_{\rm res} = 150$ MeV, and $\epsilon'_{\rm res} = (m_\Delta^2 - m_p^2)/(2m_p) \simeq 340$ MeV [66].

APPENDIX C: PROPAGATION IN THE SOURCE ENVIRONMENT

In our simple model we consider interactions and escape of particles treating the source environment as a leaky box. If at a given time, t_0, $N(t = t_0) = N_0$ particles are injected at random into the source environment, then the number of particles N remaining in the source at any later time t changes as

$$\frac{dN}{dt} = -\frac{1}{\tau_{\rm esc}} N - \frac{1}{\tau_{\rm int}} N, \tag{C1}$$

where $\tau_{\rm esc}$ and $\tau_{\rm int}$ are the escape and interaction times, respectively. Integration yields the time evolution of N as

$$N(t) = N_0 \mathrm{e}^{-\frac{t-t_0}{\tau}}, \tag{C2}$$

where

$$\tau = \frac{\tau_{\rm esc}\tau_{\rm int}}{\tau_{\rm esc} + \tau_{\rm int}}. \tag{C3}$$

The total number of escaping particles is given by

$$\begin{aligned} N_{\rm esc} &= \int_{t_0}^{\infty} \frac{1}{\tau_{\rm esc}} N(t) dt = N_0 \frac{\tau_{\rm int}}{\tau_{\rm esc} + \tau_{\rm int}} \\ &= N_0 \frac{1}{1 + \tau_{\rm esc}/\tau_{\rm int}} \equiv N_0 f_{\rm esc} \end{aligned} \tag{C4}$$

and likewise the number of particles suffering interactions is

$$N_{\rm int} = N_0 \frac{\tau_{\rm esc}}{\tau_{\rm esc} + \tau_{\rm int}} = N_0 \frac{1}{1 + \tau_{\rm int}/\tau_{\rm esc}} \equiv N_0 f_{\rm int}, \tag{C5}$$

with $N_{\rm esc} + N_{\rm int} = N_0$. As can be seen, $N_{\rm esc}$ and $N_{\rm int}$ depend only on the ratio of the escape and interaction times, but not on the absolute value of either of them.

In the following we consider sources at steady state, i.e. sources which are active long enough to justify integrating to infinity in Eq. (C4) and for which the injected flux equals the escaping flux. Interacting particles constitute the source for secondary particles of lower mass number.

Since the particle trajectory in the source is treated as a random walk starting from a random position, the escape time of a secondary does not depend on the time it was produced. Therefore we can apply Eqs. (C1) to (C5) also to the secondary particle production, which greatly simplifies the equations with respect to previous analytic approaches that had been developed for the extra-galactic propagation of cosmic-ray nuclei [79–82].

1. Single-nucleon emission

The basic principle of the analytic calculation can be best illustrated by first describing the case where interactions with the photon field lead to the knock-out of a single nucleon,

$$A + \gamma \to (A-1) + n/p, \tag{C6}$$

and the nucleon carries away a fraction of $1/A$ of the initial energy of the nucleus. This approach has been successfully applied to the photo-disintegration (PD) during the extra-galactic propagation of nuclei (see e.g. [79]). It can also serve as a good approximation for the losses due to photo-pion production (PP) if nuclei are treated as the superposition of A individual nucleons (see e.g. [83,84]). The interaction time is therefore the combination of the two processes, i.e.

$$\tau_{\rm int} = \frac{\tau_{\rm int}^{\rm PD} + \tau_{\rm int}^{\rm PP}}{\tau_{\rm int}^{\rm PD}\tau_{\rm int}^{\rm PP}}. \tag{C7}$$

In this simplified propagation scheme, secondaries with mass A and energy E^* originate from nuclei with energy $E' = \frac{A+1}{A} E^*$ and mass $A+1$. They are produced at a rate

$$\begin{aligned} \mathcal{Q}(E^*, A) &= \mathcal{Q}_{\rm int}\left(\frac{A+1}{A}E^*, A+1\right)\left|\frac{dE'}{dE^*}\right| \\ &= \mathcal{Q}\left(\frac{A+1}{A}E^*, A+1\right)\eta_{\rm int}\left(\frac{A+1}{A}E^*, A+1\right) \\ &\quad \times \frac{A+1}{A}, \end{aligned} \tag{C8}$$

where the factor $|\frac{dE'}{dE^*}|$ is the Jacobian determinant needed to transform the differential injection rate from the primary to secondary energy. In analogy to Eq. (C4), a fraction of the secondaries escapes the source environment,

$$\mathcal{Q}_{\rm esc}(E^*, A) = \mathcal{Q}(E^*, A)\eta_{\rm esc}(E^*, A), \tag{C9}$$

and the remaining particles interact again at a rate of

$$\mathcal{Q}_{\rm int}(E^*, A) = \mathcal{Q}(E^*, A)\eta_{\rm int}(E^*, A). \tag{C10}$$

This assumes that the escape probability of a secondary is independent of the time or position it got produced in the source environment. This calculation can be iterated to obtain the escape rate of any remnant with mass A^* produced during the propagation of a nucleus of mass A':

$$\mathcal{Q}^{\rm rem}_{\rm esc}(E^*,A^*,A') = \mathcal{Q}\left(\frac{A'}{A^*}E^*,A'\right)\frac{A'}{A^*}\eta_{\rm esc}(E^*,A^*) \times \prod_{A^\diamond=A^*+1}^{A'}\eta_{\rm int}\left(\frac{A^\diamond}{A^*}E^*,A^\diamond\right). \quad \text{(C11)}$$

The rate of nucleons being knocked out of nuclei during propagation via either of the considered processes $i = \mathrm{PD/PP}$ is

$$\mathcal{Q}^{i}_{\rm esc}(E^*,n+p,A') = \mathcal{Q}\left(\frac{A'E^*}{\kappa_i},A'\right)\frac{A'}{\kappa_i}\sum_{A^\oplus=2}^{A'} f_i\left(\frac{A^\oplus E^*}{\kappa_i},A^\oplus\right) \times \prod_{A^\diamond=A^\oplus}^{A'}\eta_{\rm int}\left(\frac{A^\diamond E^*}{\kappa_i},A^\diamond\right) \quad \text{(C12)}$$

with elasticities of the knock out nucleon given by $\kappa_{\rm PD} = 1$ and $\kappa_{\rm PP} = 0.8$ and the fractional contribution from PD and PP given by

$$f_{\rm PD} = \frac{1}{1+\tau_{\rm PD}/\tau_{\rm PP}}, \quad \text{and} \quad f_{\rm PP} = 1 - f_{\rm PD} = \frac{1}{1+\tau_{\rm PP}/\tau_{\rm PD}}. \quad \text{(C13)}$$

The total escape rate of particles of mass A^* from injected nuclei of mass A' is

$$\mathcal{Q}^{\rm tot}_{\rm esc}(E^*,A^*,A') = \mathcal{Q}^{\rm rem}_{\rm esc}(E^*,A^*,A') + \delta_{A^*1}[\mathcal{Q}^{\rm PD}_{\rm esc}(E^*,A^*,A') + \mathcal{Q}^{\rm PP}_{\rm esc}(E^*,A^*,A')], \quad \text{(C14)}$$

where δ_{A1} is the Kronecker delta.

2. Branching ratios from photo-disintegration

The propagation scheme described in the last section can be easily extended to take into account the emission of several nucleons or light nuclei in photo-nuclear reactions. We use the total interaction time and branching ratios for photo-dissociation from TALYS [43,44] as available in CRPROPA and neglect multinucleon emission for photo-pion production since it can be safely neglected at the energies relevant here.

Instead of the closed formulas derived above for the single-nucleon case, we now have the following recursive relation for the rate of produced remnant nuclei of mass A^*.

$$\mathcal{Q}(E^*,A^*) = \sum_{i=1}^{A'-A^*} b(E_i,A^*,A_i)\eta_{\rm int}(E_i,A_i)\mathcal{Q}(E_i,A_i)\left|\frac{dE_i}{dE^*}\right| \quad \text{(C15)}$$

with $A_i = A^* + i$, $E_i = A_i/A^*E^*$ and $|\frac{dE_i}{dE^*}| = A_i/A^*$. $b(E_i,A^*,A_i)$ is the branching ratio that gives the probability that a nucleus of mass A_i with energy E_i will have a remnant mass of A^* after the interaction. The n knocked out nucleons and nuclei are calculated the same way but replacing the branching fraction by $nb(E_i,nA^*,A_i)$, i.e. the probability to produce n fragments of mass A^*, and summing over n. The rest of the calculation proceeds as in the case of single-nucleon emission.

3. Proton interactions

Once nucleons are generated in photo-disintegration they are assumed to either escape immediately in the case of neutrons, or to interact further via photo-pion production. The average elasticity of this process is $\kappa_{\rm PP} = 0.8$ and corresponds to a shift in energy of $\Delta \lg E = \lg \kappa_{\rm PP} \approx 0.1$. Since we perform the calculation in logarithmic bins of this width, proton interactions can be treated similarly to photo-disintegration as a "trickle-down" of particles fluxes subsequently shifted by one energy bin. For the reaction $p+\gamma \to \pi^+ + n$, the neutron escapes and the interaction chain is finished. In case of $p+\gamma \to \pi^0 + p$, the secondary proton has a reduced energy; it may also interact again. The neutron, proton and positive pion fluxes in an energy bin k are calculated from the recursive relations

$$\mathcal{Q}(E^*_k,n)' = \mathcal{Q}(E^*_k,n) + (1-b_{pp})\eta_{\rm int}(E^*_{k+1},p)\mathcal{Q}(E^*_{k+1},p)'/\kappa \quad \text{(C16)}$$

$$\mathcal{Q}(E^*_k,p)' = \mathcal{Q}(E^*_k,p) + b_{pp}\eta_{\rm int}(E^*_{k+1},p)\mathcal{Q}(E^*_{k+1},p)'/\kappa \quad \text{(C17)}$$

and

$$\mathcal{Q}(E^*_k,\pi^+)' = (1-b_{pp})\eta_{\rm int}(E^*_{k+7},p)\mathcal{Q}(E^*_{k+7},p)'/(1-\kappa), \quad \text{(C18)}$$

where $b_{pp} \approx 0.5$ is the branching fraction of the process $p+\gamma \to \pi^0 + p$ and the unprimed fluxes are the sum of the knocked-out nucleons from Eq. (C15) and primary protons. The offset of 7 in the equation for the pion flux is due to the energy shift of the pions, $\Delta \lg E = \lg(1-\kappa_{\rm PP}) \approx 0.7$.

APPENDIX D: COSMIC RAY PRODUCTION AND PROPAGATION IN AN EXPANDING UNIVERSE

To compare the spectra obtained in the last section, the particles need to be propagated to Earth. The number of cosmic rays per unit volume and energy in the present universe is equal to the number of particles accumulated during the entire history of the universe and is comprised of both primary particles emitted by the sources and secondaries produced in the photo-disintegration process.

Herein, the variable t characterizes a particular age of the universe and t_H indicates its present age. We adopt the usual concordance cosmology of a flat universe dominated by a cosmological constant, with $\Omega_\Lambda \approx 0.69$ and a cold dark matter plus baryon component $\Omega_m \approx 0.31$ [86]. The Hubble parameter as a function of redshift z is given by $H^2(z) = H_0^2[\Omega_m(1+z)^3 + \Omega_\Lambda]$, normalized to its value today, $H_0 = 100\, h\,\mathrm{km\,s^{-1}\,Mpc^{-1}}$, with $h \simeq 0.68$ [86]. The dependence of the cosmological time with redshift can be expressed via $dz = -dt(1+z)H(z)$. The comoving space density of cosmic rays $n_{\rm CR}$ of mass A from a population of uniformly distributed sources with (possibly age-dependent) emission rate per volume $\mathcal{Q}(E', A', t)$ is given by

$$n_{\rm CR}(E, A, A') \equiv \frac{dN_{\rm CR}}{dE dV} = \int_E^\infty \int_0^{t_H} \frac{d\mathcal{P}_{AA'}(E', E, t)}{dE} \mathcal{Q}(E', A', t)\xi(t) dE' dt, \tag{D1}$$

where $d\mathcal{P}_{AA'}/dE$ is the expectation value for the number of nuclei of mass A in the energy interval $(E, E + dE)$ which derive from a parent of mass A' and energy E' emitted at time t, and $\xi(t)$ is the ratio of the product of comoving source density and $\mathcal{Q}(E', A', t)$, relative to the value of that product today. Note that $d\mathcal{P}_{AA'}/dE$ includes propagation effects both at the source environment and *en route* to Earth.

We assume that the emission rate of cosmic rays is the same for all sources and the spectrum and composition is independent of the age of the universe, so that evolution of the volumetric emission rate with cosmological time can be described by an overall source evolution factor, $\xi(t)$ discussed below. (It need not be specified whether this is due to an evolution of the number of sources or their intrinsic power.) We further assume, as per usual practice, that emission rate is fairly well described by a power-law spectrum. Under these general assumptions the source emission rate per volume takes the form

$$\mathcal{Q}(E', A') = \mathcal{Q}_0 \left(\frac{E'}{E_0}\right)^\gamma \exp\left(-\frac{E'}{Z' E^p_{\rm max}}\right), \tag{D2}$$

where $E^p_{\rm max}$ is the maximal energy of emitted protons, i.e., maximum rigidity of the accelerator, Z' is the nucleus' atomic number, E_0 is some reference energy, and

$$\mathcal{Q}_0 = \begin{cases} \dot{n}_0 \frac{dN_{A'}}{dE'}\Big|_{E'=E_0}, & \text{for bursting sources} \\ n_0 \frac{dN_{A'}}{dE' dt}\Big|_{E'=E_0}, & \text{for steady sources} \end{cases}. \tag{D3}$$

Here, $\dot{n}_0$ is the number of bursts per unit volume per unit time and $dN_{A'}/dE'$ is the spectrum of particles produced by each burst, or for a steady source n_0 is the number density of sources at $z = 0$, and $dN_{A'}/dE'dt$ is the UHECR production rate per unit energy per source. The cosmic ray power density above a certain energy $E'_{\rm min}$ is given by

$$\begin{aligned} \dot{e}_{E'}(A') &= \int_{E'_{\rm min}}^\infty E' \mathcal{Q}(E', A') dE' \\ &= \mathcal{Q}_0 \int_{E'_{\rm min}}^\infty E' \left(\frac{E'}{E_0}\right)^\gamma \exp\left(-\frac{E'}{Z' E^p_{\rm max}}\right) dE' \\ &= Z' E^p_{\rm max} \left(\frac{Z' E^p_{\rm max}}{E_0}\right)^{\gamma+1} \int_{E'_{\rm min}/(Z' E^p_{\rm max})}^\infty t^{\gamma+1} \mathrm{e}^{-t} dt \\ &= \mathcal{Q}_0 E_0^2 \left(\frac{Z' E^p_{\rm max}}{E_0}\right)^{\gamma+2} \Gamma\left(\gamma + 2, \frac{E'_{\rm min}}{Z' E^p_{\rm max}}\right), \end{aligned} \tag{D4}$$

where Γ denotes the upper incomplete gamma function.

The cosmological evolution of the source density per comoving volume is parametrized as

$$n_{\rm s}(z) = n_0 \xi(z) \tag{D5}$$

with $\xi(z = 0) = 1$. We adopt for the fiducial model that the evolution of sources follows the star formation rate with

$$\xi(z) = \frac{(1+z)^a}{1 + [(1+z)/b]^c} \tag{D6}$$

where $a = 3.26 \pm 0.21$, $b = 2.59 \pm 0.14$ and $c = 5.68 \pm 0.19$ [50]. Additionally we consider the family of evolution models parametrized as $\xi(z) = (1+z)^m$.

To propagate the particles escaping the source environment to Earth we use the CRPropa framework [83,84]. For this purpose, we generate a library of propagated nuclei with $A^* = 1 \ldots A^*_{\rm max}$ injected uniformly in light-travel distance. The latter corresponds to a nonevolving source distribution in comoving distance after accounting for the cosmological time dilation. We simulated particles up to $A^*_{\rm max} = 56$. Given this library of simulated particles, we can construct the propagation matrix $\mathcal{M}_{ij\mu\nu}$ for arbitrary source evolutions for each nuclear mass A^*_μ escaping the source and secondary mass A_ν at Earth. The elements of the propagation matrix give the expected number of secondaries in an energy interval $[\lg E_j, \lg E_j + \Delta]$ at Earth originating from nuclei at the source at an energy $[\lg E^*_i, \lg E^*_i + \Delta]$ for a given source evolution $\xi(z(t))$ and a uniform logarithmic spacing in energy with $\Delta = 0.1$. Numerically, the elements are constructed via discretization of Eq. (D1)

$$n_{\rm CR}(E_j,A_\nu,A') = \sum_{A^*_\mu=A_\nu}^{A'}\sum_{i=j}^{n_i}\sum_{a=0}^{n_a}\frac{\Delta\mathcal{P}_{ij\mu\nu a}}{\Delta E_j}\mathcal{Q}^{\rm tot}_{\rm esc}(E^*_i,A^*_\mu,A')\xi(t_a)\Delta t_a\Delta E^*_i, \tag{D7}$$

where $\Delta t_a = t_H/n_a$ and

$$\frac{\Delta\mathcal{P}_{ij\mu\nu a}}{\Delta E_j} = \frac{1}{\Delta E_j}\frac{N^{\rm Earth}_{ij\mu\nu a}(E^*_i,E^*_i+\Delta E^*_i;E_j,E_j+\Delta E_j;A^*_\mu;A_\nu;t_a,t_a+\Delta t_a)}{N^{\rm gen}_{i\mu a}(E^*_i,E^*_i+\Delta E^*_i;A^*_\mu;t_a,t_a+\Delta t_a)} \tag{D8}$$

For a nonevolving injection rate per unit volume, the number of generated events per bin is constant, $N^{\rm gen}_{i\mu a} = K^{\rm gen}_{i\mu}$. Then, for any source evolution $\xi[z(t))]$, (D7) can be rewritten as

$$\begin{aligned}
n_{\rm CR}(E_j,A_\nu,A') &= \sum_{A^*_\mu=A_\nu}^{A'}\sum_{i=j}^{n_i}\mathcal{Q}^{\rm tot}_{\rm esc}(E^*_i,A^*_\mu,A')\frac{\Delta E^*_i}{\Delta E_j}\sum_{a=0}^{n_a}\frac{N^{\rm Earth}_{ij\mu\nu a}}{N^{\rm gen}_{i\mu a}}\xi[z(t_a)]\Delta t_a \\
&= \sum_{A^*_\mu=A_\nu}^{A'}\sum_{i=j}^{n_i}\mathcal{Q}^{\rm tot}_{\rm esc}(E^*_i,A^*_\mu,A_\nu)\frac{\Delta E^*_i}{\Delta E_j}t_H\frac{\sum_{a=0}^{n_a}N^{\rm Earth}_{ij\mu\nu a}\xi[z(t_a)]}{n_aK^{\rm gen}_{i\mu}} \\
&= \sum_{A^*_\mu=A_\nu}^{A'}\sum_{i=j}^{n_i}\mathcal{Q}^{\rm tot}_{\rm esc}(E^*_i,A^*_\mu,A')\frac{\Delta E^*_i}{\Delta E_j}t_H\frac{\sum_{a=0}^{n_a}N^{\rm Earth}_{ij\mu\nu a}\xi[z(t_a)]}{\sum_{a=0}^{n_a}N^{\rm gen}_{i\mu a}} \\
&= \sum_{A^*_\mu=A_\nu}^{A'}\sum_{i=j}^{n_i}\mathcal{Q}^{\rm tot}_{\rm esc}(E^*_i,A^*_\mu,A')\frac{\Delta E^*_i}{\Delta E_j}t_H\frac{\sum_{p=0}^{N^{\rm Earth}_{ij\mu\nu}}\xi[z(t_p)]}{N^{\rm gen}_{i\mu}} \\
&= \sum_{A^*_\mu=A_\nu}^{A'}\sum_{i=j}^{n_i}\frac{\Delta E^*_i}{\Delta E_j}t_H\mathcal{M}_{ij\mu\nu}\mathcal{Q}_{i\mu},
\end{aligned} \tag{D9}$$

where $\sum_{p=0}^{N^{\rm Earth}_{ij\mu\nu}}\xi[z(t_p)]$ denotes the ξ-weighted sum over all events generated with (A^*_μ,E^*_i) arriving at Earth with (A_ν,E_j) and $N^{\rm gen}_{i\mu}$ is the total number of generated events with (A^*_μ,E_i). Note that if binned in $\Delta z_b = z_{\rm max}/b$, then $N^{\rm gen}_{i\mu b}|\Delta z_b/\Delta t_b| =$ constant, and hence (D9) can be rewritten as

$$n_{\rm CR}(E_i,A_\nu,A') = \sum_{A^*_\mu=A_\nu}^{A'}\sum_{i=j}^{n_i}\mathcal{Q}^{\rm tot}_{\rm esc}(E^*_i,A^*_\mu,A')\frac{\Delta E^*_i}{\Delta E_j}z_{\rm max}\frac{\sum_{a=0}^{n_a}N^{\rm Earth}_{ij\mu\nu a}\xi(z_b)}{\sum_{a=0}^{n_a}N^{\rm gen}_{i\mu a}|\frac{\Delta z_a}{\Delta t_a}|}, \tag{D10}$$

where $|\Delta z_b/\Delta t_b| = (1+z_b)H(z_b)$ and $z_{\rm max} = \Delta z_b n_b$.

For a given spectrum of injected nuclei of mass A' we obtain the space density of cosmic rays at Earth with energy E and mass A,

$$n_{\rm CR}(E,A,A') = \frac{dN_{\rm CR}}{dEdV}. \tag{D11}$$

For an isotropic arrival direction distribution (which is an excellent approximation based on current observations) the relation between the spectrum and the cosmic ray density is

$$J(E,A,A') \equiv \frac{dN_{\rm CR}}{dEdAdtd\Omega} = \frac{c}{4\pi}n_{\rm CR}(E,A,A'). \tag{D12}$$

The total flux at earth of particles of mass A_ν is

$$J(E,A_\nu) = \sum_{A'_\mu=A_\nu}^{A'_{\rm max}}f(A'_\mu)J(E,A_\nu,A'_\mu), \tag{D13}$$

where $f(A'_\mu)$ denotes the fraction of particles of mass A'_μ injected at the source.

APPENDIX E: NEUTRINO AND PHOTON PRODUCTION

The results of the last two sections can be readily applied to obtain the flux of neutrinos at Earth from the decay of neutrons and charged pions. We approximate the emission rate of pions from photo-pion production by using $\kappa_\pi = 1-\kappa_{\rm PP}$ in Eq. (C12). The energies of neutrinos escaping from the source are given by the kinematics of

the two-body decay of pions and the subsequent muon decay which we treat approximately by assigning a third of the muon energy to each of the decay products. In this way we construct a propagation matrix for pions, $\mathcal{M}_{ij\mu\nu}$ with ${}_\nu = (\nu_\mu, \bar{\nu}_\mu, \nu_e(\bar{\nu}_e))$ and ${}_\mu = \pi^\pm$. Similarly, a propagation matrix for neutrons is obtained with ${}_\nu = (\bar{\nu}_e)$ and ${}_\mu = n$.

Neutrino oscillation over astronomical distances modifies the initial flavor distribution of fluxes, Φ_e^0: Φ_μ^0: Φ_τ^0, in calculable ways. The relevant parameters for such a calculation are the three Euler rotations (θ_{12}, θ_{23}, θ_{13}) and the CP-violating Dirac phase δ. The current best-fit values as well as the allowed ranges of the mixing parameters at the 1σ level are: $\theta_{12}/^\circ = 33.57^{+0.77}_{-0.75}$, $\theta_{23}/^\circ = 41.9^{+0.5}_{-0.4} \oplus 50.3^{+1.6}_{-2.5}$, $\theta_{13}/^\circ = 8.73^{+0.35}_{-0.36}$, $\delta/^\circ = 266^{+55}_{-55}$ [87]. The mixing probabilities are given by

$$\begin{aligned} P_{\nu_\mu\to\nu_\mu} &= c_{13}^4 s_{23}^4 \\ &\quad + (c_{12}^2 c_{23}^2 + s_{12}^2 s_{13}^2 s_{23}^2 - 2c_{12}c_{23}s_{12}s_{13}s_{23}c_\delta)^2 \\ &\quad + (c_{23}^2 s_{12}^2 + c_{12}^2 s_{13}^2 s_{23}^2 + 2c_{12}c_{23}s_{12}s_{13}s_{23}c_\delta)^2, \end{aligned} \tag{E1}$$

$$\begin{aligned} P_{\nu_e\leftrightarrow\nu_\mu} &= 2c_{13}^2\{c_{12}^2 s_{12}^2 c_{23}^2 + (c_{12}^4 + s_{12}^2)s_{13}^2 s_{23}^2 \\ &\quad + c_{12}s_{12}c_{23}s_{23}c_\delta(c_{12}^2 - s_{12}^2)s_{13}\}, \end{aligned} \tag{E2}$$

$$\begin{aligned} P_{\nu_e\leftrightarrow\nu_\tau} &= P_{\nu_e\leftrightarrow\nu_\mu}(\theta_{23}\to\theta_{23}+\pi/2), \\ P_{\nu_\tau\to\nu_\tau} &= P_{\nu_\mu\to\nu_\mu}(\theta_{23}\to\theta_{23}+\pi/2), \end{aligned} \tag{E3}$$

and the unitarity relations

$$\begin{aligned} P_{\nu_e\to\nu_e} &= 1 - P_{\nu_e\leftrightarrow\nu_\mu} - P_{\nu_e\leftrightarrow\nu_\tau} \\ P_{\nu_\tau\leftrightarrow\nu_\mu} &= 1 - P_{\nu_e\leftrightarrow\nu_\mu} - P_{\nu_\mu\to\nu_\mu} \\ P_{\nu_\tau\to\nu_\tau} &= 1 - P_{\nu_e\leftrightarrow\nu_\tau} - P_{\nu_\mu\leftrightarrow\nu_\tau}, \end{aligned} \tag{E4}$$

where $c_{ij} = \cos\theta_{ij}$, $s_{ij} = \sin\theta_{ij}$, and $c_\delta = \cos\delta$ [88]. The measurable neutrino flux at Earth is given by

$$\begin{pmatrix} \Phi_e \\ \Phi_\mu \\ \Phi_\tau \end{pmatrix} = \begin{pmatrix} 0.55 & 0.24 & 0.21 \\ 0.24 & 0.37 & 0.38 \\ 0.21 & 0.38 & 0.41 \end{pmatrix} \begin{pmatrix} \Phi_e^0 \\ \Phi_\mu^0 \\ \Phi_\tau^0 \end{pmatrix}. \tag{E5}$$

In addition to neutrinos, photons are produced from π^0 production and decay [89], and by photo-disintegration of high-energy nuclei followed by immediate photo-emission from the excited daughter nuclei [90]. The γ-rays, electrons, and positrons produced in the decay of π^0 and $\pi^\pm$ trigger an electromagnetic (EM) cascade on the cosmic microwave background, which develops via repeated e^+e^- pair production and inverse Compton scattering. Other contributions to the cascade are provided by Bethe-Heitler production of e^+e^- pairs and γ-rays emitted during the photo-disintegration process, after the photo-dissociated nuclear fragments de-excite. The net result is a pile up of γ-rays at GeV $\lesssim E_\gamma \lesssim$ TeV, just below the threshold for further pair production on the diffuse optical backgrounds. The EM energy then gets recycled into the so-called Fermi-LAT region, which is bounded by observation [91,92] to not exceed $\omega_{\rm cas} \sim 5.8\times10^{-7}$ eV/cm^3 [93]. The latest Fermi-LAT limts [92] do not significantly influence the determination of the $\omega_{\rm cas}$ upper bound of [93], because that bound is not very sensitive to the high energy bins added by [92].

The photons coming from photo-pion production in the source environment were shown to be below the Fermi-LAT bound in Section III A. To place a bound on the contribution of photons from nuclear de-excitation to the Fermi-LAT diffuse gammas, without performing an explicit calculation, we can turn to the estimate of [57] which found $\omega_{\rm cas} \approx 1.1\times10^{-7}$eV/cm^3 assuming the high-energy IceCube spectrum to be entirely due to neutron beta-decay. Since in our model the neutrino flux from neutron decay is significantly below the IceCube spectrum, the corresponding de-excitation photon contribution to the Fermi-LAT data must be far below the limit.

[1] T. Antoni *et al.* (KASCADE), Astropart. Phys. **24**, 1 (2005).
[2] D. J. Bird *et al.* (HiRes), Phys. Rev. Lett. **71**, 3401 (1993).
[3] R. U. Abbasi *et al.* (HiRes), Phys. Rev. Lett. **100**, 101101 (2008).
[4] J. Abraham *et al.* (Pierre Auger), Phys. Lett. B **685**, 239 (2010).
[5] J. Abraham *et al.* (Pierre Auger), Phys. Rev. Lett. **101**, 061101 (2008).
[6] W. D. Apel *et al.*, Astropart. Phys. **36**, 183 (2012).
[7] M. G. Aartsen *et al.* (IceCube), Phys. Rev. D **88**, 042004 (2013).
[8] S. P. Knurenko, Z. E. Petrov, R. Sidorov, I. Ye. Sleptsov, S. K. Starostin, and G. G. Struchkov (Yakutsk), arXiv: 1310.1978.
[9] V. V. Prosin *et al.* (Tunka), Nucl. Instrum. Methods Phys. Res., Sect. A **756**, 94 (2014).
[10] T. Abu-Zayyad *et al.* (HiRes-MIA), Astrophys. J. **557**, 686 (2001).
[11] D. R. Bergman and J. W. Belz, J. Phys. G **34**, R359 (2007).

[12] K.-H. Kampert and M. Unger, Astropart. Phys. **35**, 660 (2012).
[13] P. Abreu *et al.* (Pierre Auger), Astropart. Phys. **34**, 627 (2011).
[14] P. Abreu *et al.* (Pierre Auger), Astrophys. J. Suppl. Ser. **203**, 34 (2012).
[15] A. Aab *et al.* (Pierre Auger), Astrophys. J. **802**, 111 (2015).
[16] A. Aab *et al.* (Pierre Auger), Phys. Rev. D **90**, 122005 (2014).
[17] A. Aab *et al.* (Pierre Auger), Phys. Rev. D **90**, 122006 (2014).
[18] V. Berezinsky, A. Z. Gazizov, and S. I. Grigorieva, Phys. Rev. D **74**, 043005 (2006).
[19] M. Ahlers, L. A. Anchordoqui, and A. M. Taylor, Phys. Rev. D **87**, 023004 (2013).
[20] M. Fukushima (Telescope Array), EPJ Web Conf. **99**, 04004 (2015).
[21] R. Aloisio, D. Boncioli, A. di Matteo, A. F. Grillo, S. Petrera, and F. Salamida, J. Cosmol. Astropart. Phys. 10 (2015) 006.
[22] D. Allard, E. Parizot, and A. V. Olinto, Astropart. Phys. **27**, 61 (2007).
[23] D. Allard, A. V. Olinto, and E. Parizot, Astron. Astrophys. **473**, 59 (2007).
[24] D. Allard, N. G. Busca, G. Decerprit, A. V. Olinto, and E. Parizot, J. Cosmol. Astropart. Phys. 10 (2008) 033.
[25] C. De Donato and G. A. Medina-Tanco, Astropart. Phys. **32**, 253 (2009).
[26] A. M. Taylor, Astropart. Phys. **54**, 48 (2014).
[27] O. Deligny, C.R. Phys. **15**, 367 (2014).
[28] T. K. Gaisser, T. Stanev, and S. Tilav, Front. Phys. China **8**, 748 (2013).
[29] R. Aloisio, V. Berezinsky, and P. Blasi, J. Cosmol. Astropart. Phys. 10 (2014) 020.
[30] G. Giacinti, M. Kachelriess, and D. Semikoz, Phys. Rev. D **91**, 083009 (2015).
[31] D. Allard and R. J. Protheroe, Astron. Astrophys. **502**, 803 (2009).
[32] K. Kotera, D. Allard, K. Murase, J. Aoi, Y. Dubois, T. Pierog, and S. Nagataki, Astrophys. J. **707**, 370 (2009).
[33] A. Pe'er, K. Murase, and P. Meszaros, Phys. Rev. D **80**, 123018 (2009).
[34] K. Fang, K. Kotera, and A. V. Olinto, Astrophys. J. **750**, 118 (2012).
[35] K. Fang, K. Kotera, and A. V. Olinto, J. Cosmol. Astropart. Phys. 03 (2013) 010.
[36] N. Globus, D. Allard, R. Mochkovitch, and E. Parizot, Mon. Not. R. Astron. Soc. **451**, 751 (2015).
[37] E. Parizot, Nucl. Phys. B, Proc. Suppl. **256–257**, 197 (2014).
[38] K. Kotera, E. Amato, and P. Blasi, J. Cosmol. Astropart. Phys. 08 (2015) 026.
[39] A. P. Szabo and R. J. Protheroe, Astropart. Phys. **2**, 375 (1994).
[40] R. J. Protheroe and T. Stanev, Astropart. Phys. **10**, 185 (1999).
[41] L. O. Drury, P. Duffy, D. Eichler, and A. Mastichiadis, Astron. Astrophys. **347**, 370 (1999).
[42] E. Krügel, *The Physics of Interstellar Dust* (Institute of Physics Publishing, London, 2003).
[43] http://www.talys.eu.
[44] We use the "TALYS-1.6 (restored)" cross sections as described in [45].
[45] R. A. Batista, D. Boncioli, A. di Matteo, A. van Vliet, and D. Walz, J. Cosmol. Astropart. Phys. 10 (2015) 063.
[46] A. Mucke, R. Engel, J. P. Rachen, R. J. Protheroe, and T. Stanev, Comput. Phys. Commun. **124**, 290 (2000).
[47] https://github.com/CRPropa/CRPropa3-data.
[48] P. Blasi, R. I. Epstein, and A. V. Olinto, Astrophys. J. **533**, L123 (2000).
[49] W. Apel *et al.*, Phys. Rev. D **87**, 081101 (2013).
[50] B. E. Robertson, R. S. Ellis, S. R. Furlanetto, and J. S. Dunlop, Astrophys. J. **802**, L19 (2015).
[51] R. C. Gilmore, R. S. Somerville, J. R. Primack, and A. Dominguez, Mon. Not. R. Astron. Soc. **422**, 3189 (2012).
[52] B. R. Dawson *et al.* (Pierre Auger, Yakutsk, Telescope Array), EPJ Web Conf. **53**, 01005 (2013).
[53] R. Abbasi *et al.* (Pierre Auger, Telescope Array), arXiv: 1503.07540.
[54] A. Aab *et al.* (Pierre Auger), arXiv:1307.5059.
[55] P. Abreu *et al.* (Pierre Auger), J. Cosmol. Astropart. Phys. 02 (2013) 026.
[56] E. J. Ahn (Pierre Auger Collaboration), arXiv:1307.5059.
[57] L. A. Anchordoqui, Phys. Rev. D **91**, 027301 (2015).
[58] M. G. Aartsen *et al.* (IceCube), Phys. Rev. D **88**, 112008 (2013).
[59] M. G. Aartsen *et al.* (IceCube), arXiv:1412.5106.
[60] M. G. Aartsen *et al.* (IceCube), Phys. Rev. D **91**, 022001 (2015).
[61] M. Ahlers, L. A. Anchordoqui, M. C. Gonzalez-Garcia, F. Halzen, and S. Sarkar, Astropart. Phys. **34**, 106 (2010).
[62] E.-J. Ahn, R. Engel, T. K. Gaisser, P. Lipari, and T. Stanev, Phys. Rev. D **80**, 094003 (2009).
[63] S. Ostapchenko, Phys. Rev. D **83**, 014018 (2011).
[64] T. Pierog, I. Karpenko, J. M. Katzy, E. Yatsenko, and K. Werner, Phys. Rev. C **92**, 034906 (2015).
[65] T. Abu-Zayyad *et al.* (Telescope Array), Astrophys. J. **768**, L1 (2013).
[66] K. A. Olive *et al.* (Particle Data Group), Chin. Phys. C **38**, 090001 (2014).
[67] A. M. Taylor, M. Ahlers, and D. Hooper, Phys. Rev. D **92**, 063011 (2015).
[68] A. H. Rosenfeld, Ann. Rev. Nucl. Part. Sci. **25**, 555 (1975).
[69] K. Fang, K. Kotera, K. Murase, and A. V. Olinto, Phys. Rev. D **90**, 103005 (2014).
[70] N. Globus, D. Allard, and E. Parizot, Phys. Rev. D **92**, 021302 (2015).
[71] D. Veberic, Comput. Phys. Commun. **183**, 2622 (2012).
[72] F. W. Stecker, Phys. Rev. **180**, 1264 (1969).
[73] J. L. Puget, F. W. Stecker, and J. H. Bredekamp, Astrophys. J. **205**, 638 (1976).
[74] S. Karakula and W. Tkaczyk, Astropart. Phys. **1**, 229 (1993).
[75] L. A. Anchordoqui, M. T. Dova, L. N. Epele, and J. D. Swain, Phys. Rev. D **57**, 7103 (1998).
[76] L. N. Epele and E. Roulet, J. High Energy Phys. 10 (1998) 009.

[77] F. W. Stecker and M. H. Salamon, Astrophys. J. **512**, 521 (1999).
[78] E. Khan, S. Goriely, D. Allard, E. Parizot, T. Suomijarvi, A. J. Koning, S. Hilaire, and M. C. Duijvestijn, Astropart. Phys. **23**, 191 (2005).
[79] D. Hooper, S. Sarkar, and A. M. Taylor, Phys. Rev. D **77**, 103007 (2008).
[80] R. Aloisio, V. Berezinsky, and S. Grigorieva, Astropart. Phys. **41**, 73 (2013).
[81] R. Aloisio, V. Berezinsky, and S. Grigorieva, Astropart. Phys. **41**, 94 (2013).
[82] M. Ahlers and A. M. Taylor, Phys. Rev. D **82**, 123005 (2010).
[83] K.-H. Kampert, J. Kulbartz, L. Maccione, N. Nierstenhoefer, P. Schiffer, G. Sigl, and A. R. van Vliet, Astropart. Phys. **42**, 41 (2013).
[84] R. A. Batista, M. Erdmann, C. Evoli, K.-H. Kampert, D. Kuempel *et al.*, arXiv:1307.2643.
[85] L. A. Anchordoqui, J. F. Beacom, H. Goldberg, S. Palomares-Ruiz, and T. J. Weiler, Phys. Rev. D **75**, 063001 (2007).
[86] P. A. R. Ade *et al.* (Planck), arXiv:1502.01589.
[87] M. C. Gonzalez-Garcia, Phys. Dark Univ. **4**, 1 (2014).
[88] S. Pakvasa, W. Rodejohann, and T. J. Weiler, J. High Energy Phys. 02 (2008) 005.
[89] F. A. Aharonian, *Very High Energy Cosmic Gamma Radiation: A Crucial Window on the Extreme Universe* (World Scientific, Singapore, 2004), p. 495.
[90] L. A. Anchordoqui, J. F. Beacom, H. Goldberg, S. Palomares-Ruiz, and T. J. Weiler, Phys. Rev. Lett. **98**, 121101 (2007).
[91] A. A. Abdo *et al.* (Fermi-LAT), Phys. Rev. Lett. **104**, 101101 (2010).
[92] M. Ackermann *et al.* (Fermi-LAT), Astrophys. J. **799**, 86 (2015).
[93] V. Berezinsky, A. Gazizov, M. Kachelriess, and S. Ostapchenko, Phys. Lett. B **695**, 13 (2011).